

## GHIGLS: H I MAPPING AT INTERMEDIATE GALACTIC LATITUDE USING THE GREEN BANK TELESCOPE

P. G. MARTIN<sup>1</sup>, K. P. M. BLAGRAVE<sup>1</sup>, FELIX J. LOCKMAN<sup>2</sup>, D. PINHEIRO GONÇALVES<sup>1,3</sup>,  
A. I. BOOTHROYD<sup>1</sup>, G. JONCAS<sup>4</sup>, M.-A. MIVILLE-DESCHÊNES<sup>1,5</sup>, G. STEPHAN<sup>1,5,6</sup>

*Accepted for publication in The Astrophysical Journal, 2015 July 16*

### ABSTRACT

This paper introduces and describes the data cubes from GHIGLS, deep Green Bank Telescope (GBT) surveys of the 21-cm line emission of H I in 37 targeted fields at intermediate Galactic latitude. The GHIGLS fields together cover over 1000 deg<sup>2</sup> at 9'55 spatial resolution. The H I spectra have an effective velocity resolution about 1.0 km s<sup>-1</sup> and cover at least  $-450 < v_{\text{LSR}} < +250$  km s<sup>-1</sup>, extending to  $v_{\text{LSR}} < +450$  km s<sup>-1</sup> for most fields. As illustrated with various visualizations of the H I data cubes, GHIGLS highlights that even at intermediate Galactic latitude the interstellar medium is very complex. Spatial structure of the H I is quantified through power spectra of maps of the integrated line emission or column density,  $N_{\text{HI}}$ . For our featured representative field, centered on the North Ecliptic Pole, the scaling exponents in power-law representations of the power spectra of  $N_{\text{HI}}$  maps for low, intermediate, and high velocity gas components (LVC, IVC, and HVC) are  $-2.86 \pm 0.04$ ,  $-2.69 \pm 0.04$ , and  $-2.59 \pm 0.07$ , respectively. After Gaussian decomposition of the line profiles,  $N_{\text{HI}}$  maps were also made corresponding to the narrow-line and broad-line components in the LVC range; for the narrow-line map the exponent is  $-1.9 \pm 0.1$ , reflecting more small scale structure in the cold neutral medium (CNM). There is evidence that filamentary structure in the H I CNM is oriented parallel to the Galactic magnetic field. The power spectrum analysis also offers insight into the various contributions to uncertainty in the data, yielding values close to those obtained using diagnostics developed in our earlier independent analysis. The effect of 21-cm line opacity on the GHIGLS  $N_{\text{HI}}$  maps is estimated. Comparisons of the GBT data in a few of the GHIGLS fields with data from the EBHIS and GASS surveys explore potential issues in data reduction and calibration and reveal good agreement. The high quality of the GHIGLS data enables a variety of studies in directions of low Galactic column density, as already demonstrated by the *Planck* collaboration. Fully-reduced GHIGLS H I data cubes and other data products are available at [www.cita.utoronto.ca/GHIGLS](http://www.cita.utoronto.ca/GHIGLS).

*Keywords:* ISM: clouds – ISM: structure – radio lines: ISM

### 1. INTRODUCTION

The 21-cm emission line of H I is the most commonly used tracer of the three-dimensional structure of the diffuse interstellar medium (ISM). Original studies were focused on structures and kinematics within the Galactic plane of the Milky Way (Burton 1976; Kulkarni et al. 1982; Stil et al. 2006), and have been expanded to studies of the vertical structure of the disk and, more generally, gas at intermediate Galactic latitudes extending into the Galactic halo (Heiles 1976; Dickey & Lockman 1990; Kalberla & Kerp 2009; Putman et al. 2012).

The discoveries and insights gained in these studies have benefited tremendously from the all-sky LAB survey (Kalberla et al. 2005), which is beam sampled at 36' angular resolution. Stimulated by these results, the range of motivations for further H I surveys is quite sweeping.

We have used the 100-m Robert C. Byrd Green Bank

Telescope (GBT, Prestage et al. (2009)) at the National Radio Astronomy Observatory (NRAO<sup>7</sup>) for complementary studies at intermediate Galactic latitude, where often the line of sight column density is low so that the emission is not strong. This paper is to introduce, describe, and disseminate the data from our deep GBT surveys of the 21-cm line emission of H I in 37 fields at intermediate Galactic latitude, obtained mainly with the Auto-Correlation Spectrometer (ACS) over the period 2005 to 2010 (see Blagrove et al. 2010 for a preliminary report). We refer to the project by the acronym GHIGLS (GBT H I Intermediate Galactic Latitude Survey). The total area mapped is over 1000 deg<sup>2</sup> and although this comprises only about 2.5% of the sky, the judicious choice of environments sampled means that a broad range of scientific questions can be addressed, as outlined below. Compared to LAB, the GHIGLS data have a higher angular resolution of about 9' and are Nyquist sampled. We have developed observing and reduction techniques for the GBT that result in high quality spectral line data cubes (Boothroyd et al. 2011) with the requisite sensitivity for studies at low column density.

An H I spectrum, whether for a single line of sight or averaged over a region, generally has emission spread

<sup>1</sup> Canadian Institute for Theoretical Astrophysics, University of Toronto, 60 St. George Street, Toronto, ON M5S 3H8, Canada; [pgmartin@cita.utoronto.ca](mailto:pgmartin@cita.utoronto.ca)

<sup>2</sup> National Radio Astronomy Observatory, Green Bank, WV USA 24944

<sup>3</sup> Department of Astronomy & Astrophysics, University of Toronto, 50 St. George Street, Toronto, ON M5S 3H4, Canada

<sup>4</sup> Université Laval, Québec, PQ, Canada

<sup>5</sup> Institut d'Astrophysique Spatiale, CNRS (UMR8617) Université Paris-Sud 11, Bâtiment 121, Orsay, France

<sup>6</sup> I. Physikalisches Institut, Universität zu Köln, Zùlpicher Str. 77, 50937, Köln, Germany

<sup>7</sup> The National Radio Astronomy Observatory is a facility of the National Science Foundation operated under cooperative agreement by Associated Universities, Inc.

over a range of frequency, which through the Doppler effect is interpreted as radial velocity, in this paper  $v_{\text{LSR}}$  relative to the Local Standard of Rest (LSR) and hereafter denoted simply  $v$ .

### 1.1. Insights from H I data

This kinematic information in H I spectra provides essential diagnostics of various physical properties of the gas. H I gas in the local neighborhood is identifiable by its low  $|v|$ , while gas in the halo appears at both intermediate and high velocities, for example in NEP in the ranges  $-80 \leq v \leq -20 \text{ km s}^{-1}$  and  $-140 \leq v \leq -80 \text{ km s}^{-1}$ , respectively (for the GHIGLS fields, it turns out that the non-local gas is only at negative velocities.) Wakker & Woerden (2013) denote the latter two both as “high-velocity clouds.” However, for the three “components” that can be distinguished via velocity we prefer the standard terminology LVC, IVC, and HVC, respectively, because there is an underlying physical distinction between these components of interstellar gas, irrespective of the apparent kinematics. There is a component of Galactic gas with an interesting history, circulating in a “Galactic fountain” (Shapiro & Field 1976; Bregman 1980). Its distinctive motion projects into a radial velocity that often sets it apart from local LVC emission, in the IVC range. On the other hand, there is gas that appears to be of extragalactic origin (perhaps it has been in other galaxies) and is now accreting on the Galaxy and destined for interaction with Galactic gas in the halo and disk. Its radial velocity is often in the HVC range. Complex C is one such example, with a low metallicity and high deuterium-to-hydrogen ratio that point to a non-Galactic origin (Tripp et al. 2003; Sembach et al. 2004).

Surveys like GHIGLS can provide new insight into these three components, LVC, IVC, and HVC. For example, correlated dust emission corroborates this distinction. Analysis with the GHIGLS data (Planck Collaboration XXIV 2011) shows that the IVC gas has an emission signature from embedded dust with a dust-to-gas ratio comparable to the LVC, whereas for HVC there is no detectable dust emission signature, consistent with a dust-to-gas ratio at least as low as implied by the low metallicity. We note that depending on the geometry, gas with physical properties similar to IVC or HVC might appear within the LVC velocity range and so not be distinguishable by its velocity (Wakker & Woerden 2013); some other clue is then needed such as, in the case of HVC-like gas, low H I-correlated dust emission (Planck Collaboration Int. XVII 2014).

There is a long history of using the power spectrum of an image to quantify the statistical properties of intensity fluctuations and structural information, including H I (Crovisier & Dickey 1983) and thermal emission by dust (Gautier et al. 1992). This structure is linked to a turbulent cascade of kinetic energy. For H I Lazarian & Pogosyan (2000) showed that the power spectrum of a velocity channel is a complex mixture of velocity and density fluctuations. For the typical steep power spectra in the ISM, the three-dimensional spectral index of density can be obtained from power spectrum analysis at high spatial frequencies by averaging enough velocity channels that the brightness temperature fluctuations are dominated by density fluctuations; otherwise the power spectrum is too shallow by up to one in the power-law

exponent. As pointed out and illustrated by Dickey et al. (2001) using H I observations in the inner Galactic plane, different regions of the ISM could have different statistical properties projected on the sky because of different fractions of gas in the cold and warm phases of the neutral medium (CNM and WNM, respectively), different optical depth effects, and geometry. In Figure 10 from their study of turbulent molecular clouds Hennebelle & Falgarone (2012) provide a comprehensive summary of the power law exponents for different tracers of the ISM at different scales. Even for the same tracer, there is a considerable range. Compared to fields near the Galactic plane or in molecular clouds, the GHIGLS fields at intermediate Galactic latitude are relatively simple lines of sight, and yet they offer the opportunity to explore both environmental differences and the structural properties of LVC, IVC, and HVC components separately.

The H I line profile, which might consist of a number of peaks with different centroid velocities, can be segmented by Gaussian decomposition (Haud 2000; Verschuur 2004) (this can be applied to H I absorption spectra as well, Roy et al. 2013). Gaussian decomposition methods offer the opportunity to differentiate between components with different line widths (Haud & Kalberla 2007). In combination with absorption-line studies (Dickey et al. 2003; Heiles & Troland 2003), components with broad or narrow line widths have been found to arise from the WNM and CNM, respectively (Dickey & Lockman 1990; Wolfire et al. 2003; Hennebelle & Falgarone 2012). For the CNM the line width is larger than simply the thermal line width because of turbulent broadening. Such an analysis of H I data from surveys like GHIGLS can illuminate theoretical numerical modelling of the phases in the ISM (e.g., Saury et al. 2014), and vice versa, leading to a better understanding of the dynamical formation of CNM gas in a thermally bistable medium and the filling factors of the phases.

### 1.2. Dust and Gas

Observations of dust emission integrate over all dust along the line of sight, regardless of velocity. The strong dust-gas correlation seen empirically in projection at high Galactic latitude (Boulanger & Perault 1988) is consistent with a strong correlation spatially in three dimensions. The dust-gas correlation has been used extensively to infer the physical properties of dust in various environments (Deul & Burton 1992; Boulanger et al. 1996; Jones et al. 1995). Reach et al. (1994, 1998) have argued that excess infrared emission relative to H I (an excess “dust emissivity”) toward brighter cloud structures signals a phase transition to  $\text{H}_2$ , untraced by CO at those column and volume densities. Subsequent all-sky observations (Planck Collaboration XIX 2011) indicate that such “CO-dark” gas is an important component widespread in the Galaxy.

The kinematic content of the H I spectra is important for decoding information in dust emission maps. Morphological spatial detail in maps of H I varies as a function of velocity and so any dust closely correlated with a velocity component of the gas leaves a related morphological imprint in the dust emission map. This approach has been used to show that there is dust of significant emissivity associated with IVC gas (Martin et al. 1994).

The selection of fields targeted by GHIGLS enables ex-

ploration of the different kinematics and spatial distributions of H I gas and the dust evolution at diverse stages of Galactic evolution. GHIGLS data have been used in combination with *Planck* data on thermal dust emission to find the emissivity, opacity, and temperature of dust associated with both LVC and IVC gas (Planck Collaboration XXIV 2011). Pinheiro Gonçalves (2013); Pinheiro Gonçalves et al. (2013) extend the analysis to emissivities characterizing non-equilibrium dust emission in the mid-infrared IRAS bands (see also Pinheiro Gonçalves, D. et al. 2015, in preparation).

Miville-Deschênes et al. (2005) have reported thermal dust emission associated with the HVC gas in the *Spitzer* First Look Survey (FLS) field. (The GBT Spectral Processor (SP) H I data used are described in Lockman & Condon 2005; they have been reprocessed here.) However, this is challenging because the dust emissivity of this lower metallicity extragalactic gas has apparently been depressed by a lower dust to gas ratio and also potentially by a lower dust temperature. Furthermore, chance correlation of the foreground LVC and IVC dust emission with the cosmic infrared background fluctuations or “anisotropies” (thus CIBA), which so far have not been separated from the dust maps, is a significant source of systematic uncertainty and no HVC-correlated dust emission has been found in the GHIGLS fields (Planck Collaboration XXIV 2011).

From another perspective, dust emission in the Galaxy is a significant foreground contamination of the CIBA signal. However, by exploiting the tight relation between Galactic dust and gas emission at low column densities, H I-correlated dust emission can be removed from the infrared and submillimeter maps, as done for COBE (Arendt et al. 1998). In combination with *Planck* and *Spitzer* data, GHIGLS data have been used for “cleaning” in this way to facilitate analysis of the residual CIBA (Planck Collaboration XVIII 2011; Pénin et al. 2012; Planck Collaboration XXX 2014).

Dust emission also contaminates measurements of the cosmic microwave background, for example compromising detection of a polarized B-mode signal from inflation (Planck Collaboration Int. XXX 2014; BICEP2/Keck Array and Planck Collaborations 2015). The Galactic magnetic field tends to be oriented parallel to the elongation of filamentary dust structures (Planck Collaboration Int. XXXII 2014; Planck Collaboration Int. XXXV 2015). Filamentary gas structures in the cold neutral medium might also be useful in tracing the orientation of the magnetic field, another way in which H I data might contribute to a more complete understanding of the ISM both phenomenologically and physically. Clark et al. (2014) have presented observations of slender, linear H I features in the diffuse ISM at high Galactic latitude and found them to be oriented along the interstellar magnetic field as probed by starlight polarization.

The plan of the paper is as follows. The selection of the GHIGLS fields surveyed is presented in Section 2. Appendix A discusses data obtained using the GBT SP while Appendix B discusses reprocessing of archival data overlapping one of these fields obtained using the GBT ACS. Section 3 describes spectral-line mapping using the GBT and the data reduction pipeline developed to produce a data cube. Various ways of visualizing the data

in a cube are reviewed briefly in Section 4 to illustrate the GHIGLS data. Separation of emission from distinct components of gas at different velocities, LVC, IVC, and HVC, is discussed in Section 5. Section 6 discusses properties of maps of the line integral  $W_{\text{HI}}$  (proportional to column density  $N_{\text{HI}}$ ) for LVC, IVC, and HVC components. The effect of 21-cm line opacity on  $N_{\text{HI}}$  is addressed in Appendix C. Appendix D evaluates the uncertainties in the data, particularly as applied to maps of the column density  $N_{\text{HI}}$ . To explore possible issues in data calibration and reduction, GBT data in a few of the targeted GHIGLS fields are compared to data from a new generation of wide-area H I surveys, in the north EBHIS (Appendix E) and in the south GASS (Appendix F). Section 7 examines angular power spectra of the  $N_{\text{HI}}$  maps of the three components. Gaussian decomposition of line profiles is explored in Section 8. The structure of the cold neutral medium and its relationship to the Galactic magnetic field are investigated in Section 9. Section 10 summarizes our conclusions.

## 2. THE GHIGLS FIELDS

Table 1 presents the fields that we surveyed with the GBT SP (Appendix A) and the GBT ACS (since 2005), in order of increasing Galactic longitude. We also reprocessed archival data obtained with the ACS for 09A079 (Appendix B). For each field the table lists the center coordinates, adopted name, size, subfield layout where relevant (Section 3), the number of repeated observations, the noise  $\sigma_{\text{ef}}$  as measured in emission-free channels (Appendix D.1) per  $0.8 \text{ km s}^{-1}$  or  $1.0 \text{ km s}^{-1}$  channel (Section 3.1), and the scan orientation (Section 3.2), along lines of constant Galactic latitude (Galactic) or Declination (ICRS).

The raw H I spectral line data using the GBT SP are available under the following proposal numbers: GBT/02A-007, 02A-023, 02A-031, and 03B-030. Those using the GBT ACS are under GBT/05C-009, 05C-021, 06B-030, 06C-032, 07A-104, 08A-083, 08B-038, 09A-079, 09B-042, 10A-012, and 10A-078. The field names adopted here are recognizable designations for the data in the NRAO archive,<sup>8</sup> except for DFN (both CDFN and HDFN), SPIDER (DDI), UMIN (NEP42), and 09A079 for the archival data described in Appendix B.

Figure 1 shows the fields in the northern Galactic intermediate latitude sky and inserts for three southern fields, including the one ACS field in the southern sky, MC, which covers part of the Magellanic Stream. The North Celestial Pole (NCP) is marked by an “×” and those fields scanned in Equatorial coordinates can be identified by their different orientation. A “+” marks the North Ecliptic Pole (NEP). Although many fields are close neighbors, even intentionally overlapping, given their size a considerable variety of physical conditions has been probed, sometimes serendipitously but particularly because the fields were chosen with certain science goals in mind.

### 2.1. Science Goals

Below we describe some motivations for targeting particular fields for our H I surveys, building on the gen-

<sup>8</sup> [archive.nrao.edu](http://archive.nrao.edu)

**Table 1**  
The Constituent Fields in GHIGLS

Field	Name	Size	Subfield Layout	Repeats	$\sigma_{\text{ef}}^1$ [mK]	Scan and Coordinates
G056.98–81.50	MC	$6^\circ \times 5^\circ$		2	81	Galactic
G058.10+68.55	BOOTES	$12^\circ 4' \times 4^\circ$	$5 \times 1$	5(2) <sup>2,3</sup> 3/ 1(2) <sup>5</sup>	70(110) <sup>4</sup> 50/ 80(60) <sup>4</sup>	ICRS
G067.74+67.73	Necklace	$2^\circ \times 2^\circ$		2	73	Galactic
G071.00+41.47	OX3	$1^\circ 9' \times 2^\circ 4'$		1 <sup>2</sup>	90 <sup>4</sup>	Galactic
G085.33+44.28	N1 <sup>6</sup>	$5^\circ \times 5^\circ$		2 <sup>7</sup>	71	Galactic
G087.95+59.05	G86	$5^\circ \times 5^\circ$		3	59	ICRS
G088.32+34.89	FLS	$3^\circ \times 3^\circ$		8 <sup>2</sup>	82	ICRS
G091.38+47.95	MRK290	$4^\circ \times 4^\circ$		1	95	Galactic
G092.24+38.43	DRACO	$5^\circ \times 5^\circ$		3	60	ICRS
G096.27+59.91	GROTH	$2^\circ \times 2^\circ$		3 <sup>2</sup>	77 <sup>4</sup>	ICRS
G096.40+30.03	NEP	$12^\circ \times 12^\circ$	$3 \times 3$	3	64	Galactic
G115.62+30.40	UMIN	$4^\circ \times 3^\circ$		1	100	Galactic
G125.00+27.42	POL	$6^\circ \times 10^\circ$		1	111	Galactic
G125.03+37.36	POLNOR	$6^\circ \times 10^\circ$		2(1) <sup>8</sup>	75(110)	Galactic
G125.37+41.67	MRK205	$4^\circ \times 4^\circ$		1	104	Galactic
G125.89+54.84	DFN	$2^\circ \times 2^\circ$		5 <sup>2</sup>	45 <sup>4</sup>	ICRS
G132.37+47.50	SP	$5^\circ \times 5^\circ$		2	71	Galactic
G134.95+54.13	UM1	$4^\circ \times 4^\circ$		1 <sup>2</sup>	83 <sup>4</sup>	ICRS
G134.98+39.97	SPIDER <sup>6</sup>	$10^\circ \times 10^\circ$	$5 \times 5$	2/ 1 <sup>9</sup>	75/ 105	Galactic
G135.36+30.29	SPC	$12^\circ \times 9^\circ 5'$	$3 \times 2$	1/ 2 <sup>10</sup>	103/ 72	Galactic
G143.94+28.02	1H0717	$4^\circ \times 4^\circ$		1	97	Galactic
G144.25+38.56	UMA	$9^\circ \times 9^\circ$	$3 \times 3$	1	107	Galactic
G145.68+23.35	HS0624	$4^\circ \times 4^\circ$		1	101	Galactic
G147.46+44.09	UM3	$4^\circ \times 4^\circ$		1 <sup>2</sup>	82 <sup>4</sup>	ICRS
G148.65+52.21	09A079 <sup>11</sup>	$5^\circ \times 4^\circ$	irregular	1 to 4	62	Galactic
G152.31+53.31	UM2M	$4^\circ \times 4^\circ$		1 <sup>2</sup>	86 <sup>4</sup>	ICRS
G152.44+25.63	MS0700	$4^\circ \times 4^\circ$		1	101	Galactic
G155.76+37.00	UMAEAST	$10^\circ 5' \times 6^\circ$	$3 \times 1$	1	107	Galactic
G156.38+32.57	LOOP4	$4^\circ \times 4^\circ$		1	122	Galactic
G156.45+54.06	NGC3310	$4^\circ \times 4^\circ$		1	95	Galactic
G158.32+28.75	MRK9	$4^\circ \times 4^\circ$		1	96	Galactic
G164.84+65.50	AG	$5^\circ \times 5^\circ$		2	71	Galactic
G170.02–59.90	SUBA	$2^\circ \times 2^\circ$		2 <sup>2</sup>	83 <sup>4</sup>	ICRS
G172.01+26.84	MBM23	$4^\circ \times 4^\circ$		1	99	Galactic
G175.36+43.38	091346A	$4^\circ \times 2^\circ$		1 <sup>2</sup>	83 <sup>4</sup>	ICRS
G179.50+65.03	MRK421	$4^\circ \times 4^\circ$		1	95	Galactic
G223.57–54.44	CDFS	$2^\circ \times 2^\circ$		5 <sup>2</sup>	93 <sup>4</sup>	ICRS

<sup>1</sup> Average noise in emission-free channels of width  $0.8 \text{ km s}^{-1}$  (except  $1.0 \text{ km s}^{-1}$  where noted<sup>4</sup>).

<sup>2</sup> Using the GBT SP (Appendix A).

<sup>3</sup> Central  $4^\circ \times 4^\circ$  subfield with two repeats. Inner  $3^\circ 5' \times 3^\circ 5'$  three further repeats, totalling five.

<sup>4</sup> Channel spacing  $1.0 \text{ km s}^{-1}$ .

<sup>5</sup> Four overlapping  $2^\circ 5' \times 4^\circ$  subfields flanking the central GBT SP subfield symmetrically. Three repeats, except western-most only once with its central 0.24 fraction in  $\delta$  repeated twice. All regridded to  $1.0 \text{ km s}^{-1}$  channel spacing of GBT SP data.

<sup>6</sup> A DRAO Deep Field (Blagrove, K. et al. 2015, in preparation).

<sup>7</sup> From data taken at times that minimize the stray radiation correction (Appendix D.5).

<sup>8</sup> Upper 0.53 fraction of field repeated twice.

<sup>9</sup> Two repeats on the inner  $3 \times 3$  of the  $5 \times 5$  subfields.

<sup>10</sup> Three  $4^\circ \times 6^\circ$  subfields and above these three  $4^\circ \times 2^\circ 5'$  subfields; only the western pair of subfields observed twice. Additional  $1^\circ$  strips on north and west to provide an overlap with SPIDER and with POL and POLNOR, respectively.

<sup>11</sup> Reprocessed archival GBT ACS data toward the Lockman Hole (Appendix B).

eral discussion in Section 1. Abstracts of our proposals making use of the GBT ACS are also available at [library.nrao.edu/proposals](http://library.nrao.edu/proposals).

However, it can be noted, certainly in retrospect, that data obtained in a focused proposal are often useful for addressing several of the distinct science goals highlighted in others. This is illustrated by the data for many GHIGLS fields that proved useful for the above-mentioned *Planck* studies of the CIBA and Galactic dust.

### 2.1.1. Extragalactic Windows

H I surveys are used first to identify regions of low Galactic column density and then to characterize or re-

move foregrounds that otherwise compromise extragalactic science. With the GBT SP, the foreground H I has been explored in a number of extragalactic or “cosmic” windows for deep multiwavelength observations of the distant universe. The fields UM2M together with 09A079 and NGC3310 (both with the GBT ACS) overlap the Lockman Hole, the region with the lowest integrated H I emission (Figure 1). The Lockman Hole has been studied previously in H I at  $10'$  resolution using the NRAO 300-ft telescope (Lockman et al. 1986; Jahoda et al. 1990) and was an important field for the *Spitzer* SWIRE survey (Lonsdale et al. 2003) and many other studies, e.g., with XMM-Newton (Hasinger et al. 2001). UM1 has similarly

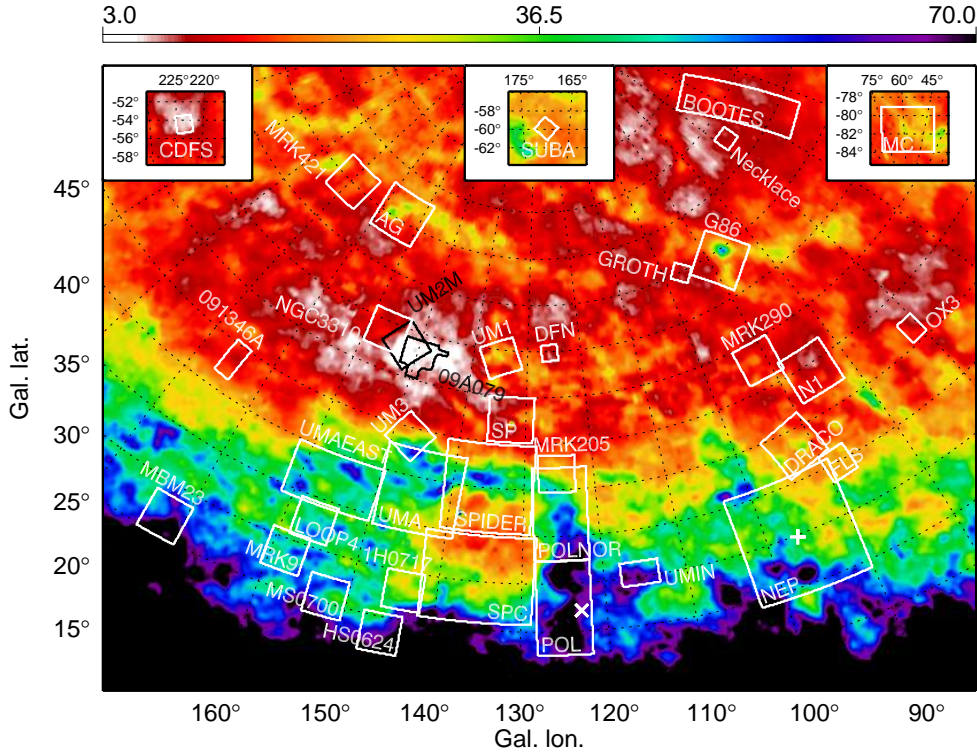


**Figure 1.** Locations of GHIGLS fields. Fields are rectangular in the local GLS projection appropriate to the OTF mapping but in this stereographic (STG) projection the outlines are slightly distorted. Background image is the velocity-integrated H I emission from the all-sky LAB survey (Kalberla et al. 2005), expressed as column density  $N_{\text{HI}}$  in units  $10^{19} \text{ cm}^{-2}$ . The North Celestial Pole (NCP) is marked by an “x” at  $122^{\circ}93, 27^{\circ}13$ . The GBT fields cover the entire NCP Loop and its interior. The North Ecliptic Pole (NEP) is marked by a “+” at  $96^{\circ}38, 29^{\circ}81$ . MC and two other southern fields are shown to scale in the insets on GLS grids.

low LVC emission, but has much brighter IVC emission and some HVC as well.

In addition to those discussed further below, BOOTES (extended with the ACS) and N1 (with the ACS), GHIGLS GBT SP fields span many other notable windows: OX3 – the Hercules field in the Oxford-Dartmouth Thirty Degree Survey (MacDonald et al. 2004); GROTH – the All-Wavelength Extended Groth Strip International Survey (AEGIS) region (Davis et al. 2007); DFN – *Chandra* Deep Field North/Hubble Deep Field North/GOODS-N (Hornschemeier et al. 2001); SUBA – the Subaru/XMM-*Newton* Deep Survey Field (Ouchi et al. 2001) (also SWIRE); and CDFS – *Chandra* Deep Field South/GOODS-S (Giacconi et al. 2001) (also SWIRE). We note that these areas include four of the five (tiny) CANDELS fields (Grogin et al. 2011).

### 2.1.2. High Velocity Infall

The European Large-Area ISO Survey (ELAIS) N1 field is an extragalactic window also targeted by SWIRE whose low column density can be appreciated in Figure 1. The complex H I structure has been studied at  $1'$  resolution using the Synthesis Telescope (ST) at the Dominion Radio Astrophysical Observatory (DRAO<sup>9</sup>), mosaicing data from 76 closely-packed pointings to produce a sensitive “DRAO Deep Field” for which our GBT ACS data, the GHIGLS N1 field, provide the short spacing information (Blagrave, K. et al. 2015, in preparation). Unlike the Lockman Hole, this region has striking HVC emis-

sion, enabling a search for HVC-correlated dust emission. The HVC gas morphology is not immediately obviously traced by dust, and in fact it turns out quantitatively, at least at the GBT angular resolution, that the HVC has a low dust emissivity (Planck Collaboration XXIV 2011).

Along with N1 and FLS, we extended our study of dust emissivity in HVC complexes by selecting regions in which the HVC to IVC plus LVC column density in the LAB survey showed a high contrast: MC, SP, and AG. (There are also significant knots of high contrast HVC emission contained within SPC, UMA, and UMAEAS.) Their low total column density makes these fields suitable for CIBA studies as well (Planck Collaboration XVIII 2011; Pénin et al. 2012; Planck Collaboration XXX 2014), but we found that the CIBA significantly contaminates studies of (HVC) H I-correlated dust emission (Planck Collaboration XXIV 2011).

### 2.1.3. The Galactic Fountain

DRACO (Herbstmeier et al. 1993) and G86 (Martin et al. 1994) were selected because of their prominent and distinctive IVC gas which has a clear dust signature. Targeted *Herschel* dust emission and DRAO ST H I observations were carried out for these two fields as well. Such fields are ideal for searching for differences in dust properties between local and IVC gas, evidence of dust evolution in different IVC environments. The dynamics is fascinating and in DRACO the transition from atomic to molecular gas can be studied.

The central region of our BOOTES field targeted the extragalactic window known as the NOAO Deep Wide

<sup>9</sup> [www.nrc-cnrc.gc.ca/eng/solutions/facilities/drao.html](http://www.nrc-cnrc.gc.ca/eng/solutions/facilities/drao.html)

Field Survey (Jannuzi & Dey 1999) and the focus of a *Spitzer* MIPS wide/shallow survey (Dole et al. 2004). It is actually crossed by a band of Galactic dust emission within which we subsequently discovered anomalously high dust emissivity in one faint component of IVC gas (Lockman et al. 2005); to explore this further, with the GBT ACS, we added flanking subfields along the direction of the band. In IRAS 60 and 100  $\mu\text{m}$  dust maps of the Böttes region there appears a remarkable feature that we dubbed the Necklace and for which we carried out a small H I survey to study the dust emissivity.

#### 2.1.4. North Ecliptic Pole Foreground

We mapped H I in a large region centered on the NEP. As far as gas and dust content is concerned, there is nothing special a priori about this intermediate latitude location. However, for many all-sky surveys by satellites that scan along great circles passing near the ecliptic poles, the NEP region is special in having more coverage and hence data products with lower uncertainty. This is the case for *Einstein*, IRAS, COBE, ROSAT, AKARI, and recently *Planck*, as illustrated in the coverage map (see, e.g., figure 5 in Planck Collaboration I 2014) and related variance maps. Thus the NEP region is the focus for many studies, e.g., recently with *Chandra* (Krumpe et al. 2015). For several science applications using these data it is important to understand the foreground from the Galaxy.

H I in this region was surveyed previously using the 140-ft telescope at NRAO (Lockman et al. 1986). Our NEP GBT ACS data cover a larger region with higher angular resolution and much reduced noise and systematic uncertainty. The observations, repeated three times, have a good signal to noise ratio, there is significant LVC, IVC, and even HVC emission, and the field is large, all reasons why we chose NEP data for illustrations in this paper.

#### 2.1.5. The North Celestial Pole Loop

The first large field targeted with the GBT ACS was SPIDER, at the top of the arch of the North Celestial Pole Loop (NCPL), a giant gas structure north of the Galactic Plane with a cylindrical morphology (see Meyerderks et al. 1991). In SPIDER the complex LVC H I structure has been studied with the DRAO ST, mosaicing data from 91 pointings to produce a second DRAO Deep Field. We have also mapped the stunning dust emission there at even higher resolution with *Herschel*.

Ultimately we explored H I throughout the spider’s web, along the entire NCPL extending from POL to UMAEAST, and also H I in its “interior” below the arch with SPC and several fields toward higher longitude. See Figure 1. POL covers the Polaris flare, which is actually dominated by molecular gas, not H I. *Herschel* dust emission maps and DRAO ST H I observations were acquired for parts of POL and UMA (Blagrove, K. et al. 2015, in preparation).

#### 2.1.6. Molecular Hydrogen

In some of the GHIGLS fields analyzed in Planck Collaboration XXIV (2011) there was evidence from excess submillimeter dust emission for gas not traced by H I, suggesting the presence of H<sub>2</sub>. To explore evolutionary

aspects of this phenomenon in relation to different environmental and kinematic factors at intermediate Galactic latitude, we focused on fields containing an AGN for which FUSE observations have been used to characterize H<sub>2</sub> (Gillmon et al. 2006; Wakker 2006) and one field containing a small, non star forming molecular cloud, MBM 23 (Magnani et al. 1985). Many of these fields have been observed with the DRAO ST as well, for which our GBT observations provide the short spacing data.

### 3. SPECTRAL-LINE MAPPING WITH THE GBT

Surveys of H I spectra in sizeable fields were carried out using on-the-fly (OTF) mapping. As described in detail by Boothroyd et al. (2011), data were acquired with the GBT ACS by in-band frequency switching, with spectra recorded every 4 s in two independent polarizations. The velocity coverage was  $-1700 \leq v \leq +900 \text{ km s}^{-1}$  in independent  $0.161 \text{ km s}^{-1}$  channels, from which was extracted the central  $-450 \leq v \leq 400 \text{ km s}^{-1}$ . With the broad spectral coverage, emission from LVC, IVC, and HVC gas is all accessible.

In our H I surveys, scans of the sky up to  $6^\circ$  long were made. For practical purposes larger fields were broken up into smaller subfields with scan dimension between  $2^\circ$  and  $4^\circ$  that were mapped separately. The scans are still sufficiently long that the choice of OTF mapping greatly reduces the system overhead. The mapping speed is typically one  $\text{deg}^2$  per hour. As described below, we mapped over 1000  $\text{deg}^2$  using the GBT ACS. Observations of many fields were repeated both to increase the sensitivity and to examine the reproducibility of the data, leading to better maps.

Aspects of the mapping, processing of the spectra, and data cubes are discussed in this section. The accuracy of the data has been discussed by Boothroyd et al. (2011) and this is complemented by the analysis in Appendix D.

#### 3.1. Processing of the Spectral Data

The desired quantity to be measured, designated simply by  $T_b$  in this paper, is the H I brightness temperature averaged over the main beam. As described by Boothroyd et al. (2011), the data reduction process involves removal of radio frequency interference (RFI), producing the frequency-switched spectra including a cubic spline interpolation of the data onto a common grid in  $v$ , spectral smoothing and resampling to  $0.807 \text{ km s}^{-1}$  channels<sup>10</sup> (or  $1.03 \text{ km s}^{-1}$ ), averaging the two polarizations, calibration of the intensity scale to antenna temperature,  $T_a$ , calculation and subtraction of the stray radiation spectrum, correction for the main beam efficiency and the atmosphere, interpolation of the sampled spectra from all repeated observations into a data cube, and finally removal of a small (low-order and low-amplitude) instrumental baseline for each interpolated spectrum in the data cube. In some cases, the presence of a galaxy makes it impossible to fit a reliable baseline and thus no baseline is removed. A mask developed for the data product release reflects these cases.

The repeated observations were also used to produce independent data cubes for diagnostic analysis (see

<sup>10</sup> We filtered the spectra with an eleven-channel Hanning kernel (nine non-zero weights) and then sampled every fifth channel to produce independent data. The effective resolution is  $1.0 \text{ km s}^{-1}$ .

Boothroyd et al. 2011 and Appendix D). Similarly, we have compared data products obtained by processing the two independent polarizations separately (Boothroyd et al. 2011) to check for reliability.

### 3.2. Mapping, Gridding, and Resulting Angular Resolution

The native primary beam of the GBT is only mildly elliptical with full width half maximum (FWHM)  $9'1$  and  $9'0$  in the cross-elevation (azimuthal) and elevation direction, respectively. The integration time (4 s) and telescope scan rate were chosen to sample the spectrum every  $3'5$  in the in-scan direction, more finely than the Nyquist interval,  $3'86$ . Beam broadening in OTF mapping can be made negligible by sampling at a smaller fraction of the Nyquist rate (Mangum et al. 2007), ideally at half that interval. Our actual sampling amounts to a convolution of the beam with a  $3'5$  boxcar, extending the beam to an effective FWHM of  $9'4$  in the in-scan direction (not aligned along either azimuth or elevation).

Fields were mapped boustrophedonically, scanning the telescope in one direction (Galactic longitude or Right Ascension), with steps of  $3'5$  in the orthogonal (cross-scan) coordinate direction before the subsequent reverse scan. The quality of the spectra was monitored closely during most sessions. Occasionally artifacts from the spectrometer would compromise a spectrum and it was flagged; usually it was possible to schedule an observation to replace the entire scan.

The individual spectra were gridded into data cubes. For these large fields, the equal-area Global Sinusoidal (GLS) coordinate projection (Calabretta & Greisen 2002) was chosen to complement our equal-area sampling strategy. GLS is now replaced by the Sanson-Flamsteed (SFL) projection, which can be considered equivalent as used here. Gridding data from a large region to another projection, like TAN, would produce pixels (spectra in the cube) with non-uniform coverage. The data are mapped to the grid following a convolution. The simplest convolution would be a pillbox, the naive-mapmaking strategy of assigning each sample to its nearest neighboring grid cell. With GLS projection, a grid can be defined with  $3'5$  pixels corresponding to where the data were sampled, in which case each pixel contains the actual spectrum recorded. This is very useful for diagnostic purposes as we assess the accumulation of error in individual spectra.

However, pillbox is not the ideal gridding for our data. Instead we used an optimal tapered Bessel function for interpolation (Mangum et al. 2007), available in Classic AIPS with the task SDGRD. This approach also allowed us to account for small telescope pointing deviations in the in-scan direction relative to the expected uniform raster. Convolution with a Bessel function, being the inverse Fourier transform of a top hat, is the equivalent of equally sampling all spatial scales in the Fourier domain with a two-dimensional boxcar function of size extending to the resolution limit  $D/\lambda = 1/7.25 \text{ arcmin}^{-1}$ . It preserves the true power on small spatial scales while avoiding the introduction of noise on scales smaller than the beam. The corresponding “width” of the Bessel function is  $3'75$ . Because the observed fields are finite (i.e., no information exists beyond the edge of the observed field), the Bessel function is tapered by a Gaussian. The sup-

port size (the radius beyond which the tapered Bessel function is truncated) was chosen to correspond to a zero intercept of the Bessel function. Both the first and second of these intercepts, corresponding to  $7'5$  and  $11'25$ , were considered. A larger support size allows for a broader Gaussian taper resulting in less modification of the beam profile; while this results in loss of information at the map edge, for our large maps this loss is inconsequential. Thus a support size of  $11'25$  was selected along with a Gaussian taper “width” (as defined in the AIPS task SDGRD) of  $9'16$ , which corresponds to a Gaussian with  $\text{FWHM} = 15'26$ . The width of the Gaussian taper is chosen to be as broad as possible, while also maintaining a smooth transition from the (otherwise infinite in nature) Bessel function to a value of zero beyond its support size (i.e., its truncation radius).

As is the case with any non-pillbox grid system, the beam ends up being broadened slightly in both in-scan and cross-scan directions. The resulting effective beam for our modified Bessel function gridded data cubes can be approximated by an elliptical Gaussian of size  $9'55 \times 9'24$  (FWHM).

Data cubes were constructed in Classic AIPS, combining spectra from the two polarizations and from repeated observations as appropriate. A weight map was created using SDGRD during convolution of the spectra into the GLS grid and this map was used to remove a few pixels along the edge of the map, leaving a cube with uniform coverage. Spectra from the subfields mapped were combined directly into a common GLS grid (with the same  $3'5$  pixel size), providing a mosaic of the entire region. Because the areas covered by the subfields are rotated slightly compared to this common grid, there is a sawtooth pattern to the weighting function along the mosaic edges. This too was removed for the final data products. These cropped mosaics have near-uniform coverage (weight), increasing where the subfields overlap.

These cubes were examined for any evidence of the effects of an anomalous spectrum that might have been missed in the previous flagging, in which case the bad spectrum was identified and flagged and the cube remade, where possible including a replacement scan; any remaining locations affected by missing/flagged spectra are identifiable in the weight and noise maps. Finally a baseline was fit to the gridded data in each pixel and subtracted. A mask was developed to record the few pixels for which a baseline fit to the spectrum was deemed not feasible, usually due to the presence of emission from a galaxy; the uncorrected spectra are still very good because of the intrinsically flat baselines of the GBT ACS.

On the archive of GHIGLS data,<sup>11</sup> for each field there is a FITS file with extensions as follows: 0, the cube of spectra  $T_b$  in K; 1, a mask recording the few pixels with no baseline fit removed (many fields do not require this extension); 2, a map of the noise  $\sigma_{ef}$  as measured in emission-free channels of each spectrum, in K, and 3, the (relative) weight map. In the noise map can be seen the reduction in noise from overlapping/repeat observations, the subfield layout where relevant (e.g., Figure 15), and the rare increases in noise because of flagged spectra. These are a direct consequence of the weighting and so appear in the weight map as well.

<sup>11</sup> [www.cita.utoronto.ca/GHIGLS](http://www.cita.utoronto.ca/GHIGLS)

### 3.3. Mosaiced Data

The data for the tabulated GHIGLS fields have been analysed separately, but to explore larger-scale connections between features in individual fields we have combined the data in some adjacent/overlapping fields into mosaics, in the same way that subfields were combined for a given target. In this reprocessing, we first ensured that the individual spectra had a common velocity grid. Then we executed the last two steps of our pipeline, interpolation of the spectra onto a common GLS grid, and removal of a small instrumental baseline fit at each pixel. FITS files of the mosaics are available on the GHIGLS archive.

We have made a small mosaic LHM covering the low column density area in the Lockman Hole region by combining the data from NGC3310, UM2M, and 09A079. Because of the overlap the sensitivity is improved over the central region, as can be seen in the noise map. Close inspection shows that of the three fields, UM2M has slight residuals from the stray radiation correction.

We have combined data for NEP, FLS, and DRACO into a mosaic named NFD. This reprocessing also includes data for a small 3 deg<sup>2</sup> map KnotN under proposal GBT/06B-030 exploring the IVC and an embedded 16 deg<sup>2</sup> field H1821 under GBT/09C-042, not documented in Table 1 or Figure 1 but evidenced in the noise map. In this mosaic it can be seen how the distinctive LVC filament in FLS extends into DRACO and is roughly parallel to the filaments already mentioned in NEP.

As Figure 1 shows, GHIGLS has extended coverage of the NCPL and so we have made a large mosaic thus named. This reprocessing also includes data from a few embedded surveys, namely KnotA, B, and C under GBT/05C-021, our exploratory focus on high-contrast HVC emission, plus fields called PG0804 under GBT/09B-042 and LISZTA, LOOP1+2, and LOOP4B under GBT/10A-012. This shows the spectacularly complex structures in the LVC emission collectively defining the arch, but also fascinating IVC and HVC emission as well.

## 4. VISUALIZATION OF A DATA CUBE

The complex H I spectral information  $T_b(x, y, v)$  assembled in a data cube can be visualized in a number of ways. The rendering<sup>12</sup> in Figure 2 for the NEP field reveals the characteristic clumpy structure of  $T_b$  in the three dimensions of the cube. We note, however, that  $v$  does not necessarily map directly into a third spatial dimension. The sense of connectedness and separation of the structures can be reinforced by interactively changing the viewing angle (azimuth and elevation). We have created a movie to illustrate this, smoothly varying the viewing angle so that the cube appears to tumble before eventually returning to the frame shown in Figure 2.

Figure 3, also for NEP, shows three complementary slices of the cube: “a channel map” and two “position-velocity diagrams.” Position-velocity diagrams reveal not only the complex structure in the gas, but also regularity such as distinct ranges in  $v$  in which the emission is concentrated (e.g., distinct LVC, IVC, and HVC are clearly

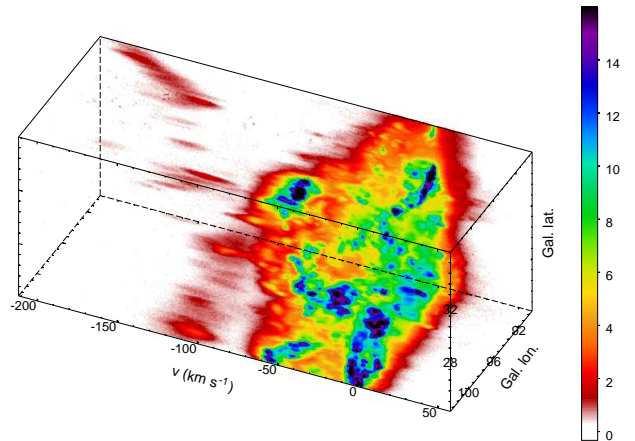


**Figure 2.** Rendering of the  $T_b(x, y, v)$  data in the spectral cube for the NEP field between  $-210$  and  $60$  km s<sup>-1</sup>. The colorbar is linear in  $T_b$  (K). Changing the viewing angle can reinforce the sense of connectedness and separation of the structures, as illustrated in a movie of a tumbling cube beginning and ending at the frame shown here ([www.cita.utoronto.ca/GHIGLS/MOVIES/TUMBLE/GHIGLS\\_NEP\\_tumble.mp4](http://www.cita.utoronto.ca/GHIGLS/MOVIES/TUMBLE/GHIGLS_NEP_tumble.mp4)<sup>a</sup>).

<sup>a</sup>All movies are also available in “ogg” format.

seen in the  $(\ell, v)$  diagram shown at the lower right). Connectivity in these diagrams, or more generally in the rendered cube, can suggest a physical relationship between the different velocity components. A sequence of channel maps (or orthogonal planes) can be combined as the frames of a movie file. For the NEP we have made three such movies, within which the images in Figure 3 are single frames (see caption). For the other GHIGLS fields, equivalent movies including tumbling cubes can be found on the GHIGLS archive.

The individual spectra at the lower left in Figure 3 can be compared to the mean spectrum for the cube in Figure 4; across the field the spectrum changes dramatically in the LVC, IVC, and HVC ranges.

A striking phenomenon seen over the LVC range of the NEP cube is a series of filamentary structures all running roughly diagonally across the field. Some of these can be seen in the single channel map in Figure 3. As discussed in Section 9, these appear to be aligned with the local Galactic magnetic field.

## 5. SEPARATING LOW, INTERMEDIATE, AND HIGH VELOCITY GAS

Separating the H I emission into contributions from LVC, IVC, and HVC gas is challenging when the velocity ranges of the components overlap. For NEP the HVC emission is relatively weak but in Figures 2 and 3, and even in the average spectrum in Figure 4, it is fairly well separated. The IVC emission is not as strong as LVC and while the existence of IVC is apparent in the average spectrum in Figure 4 it is not obvious exactly where to make the separation from LVC.

A useful diagnostic is based on the standard deviation about the mean of a channel map, because it depends not just on the presence of signal but also on the fluctuations. Thus the standard deviation spectrum takes advantage of the rich structure within the cube and so when the emission corresponding to LVC, IVC, and HVC components is not immediately distinguishable in the mean spectrum it offers the potential to separate the cube into distinct velocity ranges (Planck Collaboration XXIV 2011).

<sup>12</sup> Created with SAOImage DS9 (<http://ds9.si.edu>) using a simple ray-trace algorithm with the Maximum Intensity Projection method.



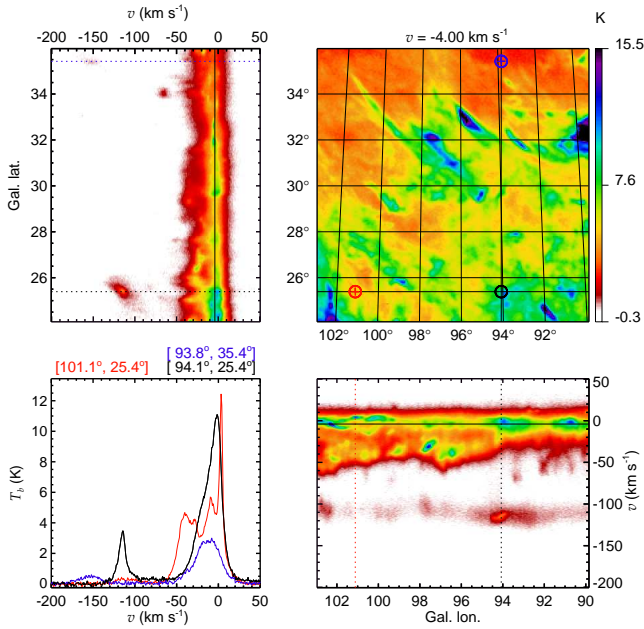


**Figure 3.** Maps of  $T_b$  on three complementary orthogonal slices of the H I spectral cube for the NEP field. Upper right: Channel map  $(\ell, b)$  at  $v = -4.0 \text{ km s}^{-1}$ , viewed from the high  $v$  face of the cube as rendered in Figure 2. This is a single frame from a movie running through channel maps of the entire cube, starting from the highest  $v$  ([www.cita.utoronto.ca/GHIGLS/MOVIES/LB/GHIGLS\\_NEP.mp4](http://www.cita.utoronto.ca/GHIGLS/MOVIES/LB/GHIGLS_NEP.mp4)). Striking filamentary structures cross the field diagonally, roughly parallel to the direction of the Galactic magnetic field (Section 9). Solid vertical or horizontal lines represent the cross-section cut from which the adjacent complementary position-velocity diagrams are built. The two position-velocity diagrams are as follows. Lower right:  $(\ell, v)$  at fixed  $b = 25.4^\circ$ ; the view is from the low- $b$  face of the cube in Figure 2 with the  $v$  axis foreshortened. This is a single frame from a movie running through  $(\ell, v)$  slices of the entire cube, starting from the lowest  $b$  ([www.cita.utoronto.ca/GHIGLS/MOVIES/LV/GHIGLS\\_NEP\\_lv.mp4](http://www.cita.utoronto.ca/GHIGLS/MOVIES/LV/GHIGLS_NEP_lv.mp4)). Vertical dashed lines mark the longitudes along which profiles of the intensity in this diagram are shown in the panel at the lower left; these profiles are the spectra at two of the pixels marked by bulls-eyes in the channel map. Upper left:  $(v, b)$  for  $\ell \sim 94^\circ$ , more precisely the plane through  $(\ell, b) = (94.1^\circ, 25.4^\circ)$ ; the view is from the high- $\ell$  face of the cube in Figure 2 with the  $v$  axis foreshortened. This is a single frame from a movie running through  $(v, b)$  slices of the entire cube, starting from the highest  $\ell$  ([www.cita.utoronto.ca/GHIGLS/MOVIES/VB/GHIGLS\\_NEP\\_vb.mp4](http://www.cita.utoronto.ca/GHIGLS/MOVIES/VB/GHIGLS_NEP_vb.mp4)). Horizontal dashed lines mark the latitudes of the spectra shown. Lower left: Distinctive individual spectra for the three pixels marked by the bulls-eyes in the channel map, along the dashed lines in the position-velocity diagrams. The spectrum at the special pixel  $(94.1^\circ, 25.4^\circ)$  can be seen in both position-velocity diagrams.

We have evaluated this approach using two cubes from the hydrodynamical simulations of the structure of the thermally bistable and mildly turbulent atomic gas in the local ISM (Saury et al. 2014). These include turbulent forcing with a mixture of compressive and solenoidal modes whose partition is set by the spectral weight  $\zeta$  (ranging from 0 for compressive to 1 for solenoidal), a turbulent forcing amplitude  $v_s$ , and initial density  $n_0$ , and for investigating the approach to component separation here, the exact choice of parameters/simulations does not matter. Each of these cubes consists only of LVC. However, we combined them by summing  $T_b(x, y, v)$  after translating one cube by  $\Delta v_{\text{shift}}$ , thus producing an IVC component as well. We added

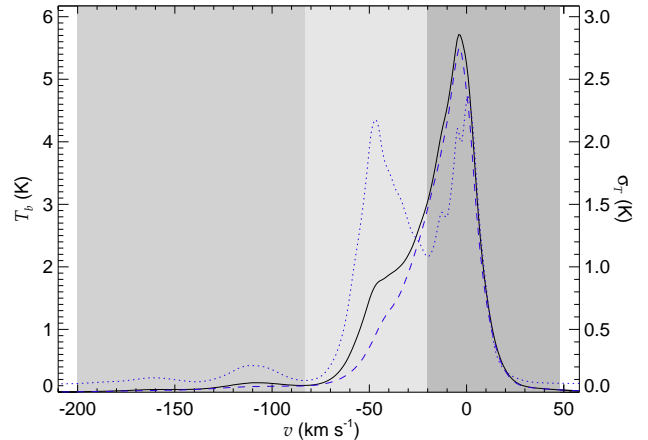


**Figure 4.** Spectral profiles of the mean (solid) and median (dashed) values of  $T_b$  for the NEP field (left axis) and of the standard deviation about the mean of  $T_b(v)$  (dotted,  $\sigma_T$ , right axis). The complexity of H I structure along the line of sight complicates the separation of the different radial velocity components. Although more blended in the mean and median profiles, the LVC, IVC, and HVC components become more distinct in the standard deviation spectrum.

noise characteristic of observations of the GBT fields. When  $\Delta v_{\text{shift}}$  exceeds the typical FWHM of the line profile, the separation of components is unambiguous, whether using the mean or standard deviation spectrum. But the separation becomes more challenging for smaller  $\Delta v_{\text{shift}}$  and the superior utility of the standard deviation spectrum is clear. We quantified this by comparing the column densities (Section 6) computed for the two ranges to the actual column densities in the original cubes. For conditions like encountered in the actual GHIGLS fields, the internal boundaries between LVC and IVC and between IVC and HVC can be determined to better than a few  $\text{km s}^{-1}$ .

The application to NEP is shown in Figure 4, from which the selected bounding velocities are  $[47.9, -20.5, -83.3, -199.9] \text{ km s}^{-1}$ . Table 2 shows the adopted velocities for component boundaries in the GHIGLS fields. These values correspond precisely to particular channels boundaries in the data cube, but depending on the field the actual internal boundaries can be uncertain by a few channels.

If the separation is ambiguous, it becomes a potential systematic error in whatever dependent analysis is being carried out and so a sensitivity analysis needs to be done. Consider the case of distinct dust emissivities associated with LVC and IVC components. Our approach has been to correlate simultaneously the LVC and IVC column density with a dust emission map from the all-sky *Planck* survey (Planck Collaboration XI 2014), with the two emissivities as free parameters. When the component separation seemed somewhat arbitrary, the velocity boundary between the LVC and IVC components was changed incrementally over the range of possible velocities, producing a pair of emissivities and an rms of the residual dust map for each case. The velocity boundary corresponding to the minimum value of the rms was consistent with that determined independently from the standard deviation spectrum. The derived values of the emissivities were robust and the uncertainty of the velocity boundary did not significantly increase the uncer-

**Table 2**  
Component Velocity Boundaries (km s<sup>-1</sup>)

Name	LVC	IVC	HVC
MC	50.4	-6.0	-39.8
BOOTES	29.5	-17.9	-69.4
Necklace	14.9	-9.2	-50.3
OX3	50.2	-28.2	-95.1
N1	57.6	-10.8	-59.9
G86	23.8	-26.9	-64.8
FLS	27.8	-19.7	-114.6
MRK290	35.1	-47.9	-80.9
DRACO	23.8	-8.4	-72.8
GROTH	27.5	-37.4	-66.3
NEP	47.9	-20.5	-83.3
UMIN	50.4	-22.9	-58.3
POL	31.8	-48.7	-97.0
POLNOR	31.8	-26.9	-97.0
MRK205	39.9	-35.0	-100.2
DFN	50.2	-28.2	-105.4
SP	31.8	-30.2	-105.0
UM1	60.5	-24.1	-93.1
SPIDER	39.9	-14.9	-88.1
SPC	32.6	-47.9	-100.2
1H0717	50.4	-36.6	-109.8
UMA	50.4	-26.1	-84.9
HS0624	39.9	-33.4	-68.0
UM3	29.5	-25.1	-84.8
09A079	60.0	-30.2	-80.1
UM2M	39.8	-30.2	-79.7
MS0700	36.7	-31.8	-100.2
UMAEAST	40.7	-18.1	-88.1
LOOP4	39.9	-22.9	-100.2
NGC3310	30.2	-30.2	-76.0
MRK9	35.1	-33.4	-70.4
AG	47.9	-31.8	-72.8
SUBA	50.2	-12.7	-79.7
MBM23	50.4	-13.3	-72.8
091346A	39.8	-23.0	-90.0
MRK421	35.1	-44.6	-120.3
CDFS	41.9	-19.9	-60.1

tainty of the emissivities. We note that this is not a test of uniqueness, but of consistency. But additionally, if the two emissivities were the same, then the motivation for finding a precise separation of LVC and IVC would be moot.

For many emissivity analyses (e.g., [Planck Collaboration XXIV 2011](#)), some of the spectral data end up masked – mostly due to the presence of unaccounted hydrogen in the form of H<sub>2</sub> or sometimes H<sup>+</sup>. In such cases, it might be beneficial to iterate on the standard deviation spectrum to determine the ideal separation between components including only the relevant data, those in the retained (not-masked) region. This has not been implemented here.

Another consideration for closely adjacent ranges is that some signal from the LVC gas can contaminate the IVC component and vice versa, because of the overlap of the extended wings of their respective line profiles. An alternative method that takes into account these “intruding” extended wings implicitly is based on Gaussian decomposition of the individual spectra (Section 8).

## 6. MAPS OF THE LINE INTEGRAL

It is informative to calculate the integral  $W_{\text{HI}}$  of the H I emission spectrum over velocity (or over distinct velocity ranges – e.g., LVC, IVC, HVC), because  $W_{\text{HI}}$  is related to the column density  $N_{\text{HI}}$ . At high latitudes, where the brightness of the infrared dust emission – the “cirrus” – is low because of low dust column density, the

high-latitude 21-cm emission is also faint, with the peak temperature of the spectral lines usually small compared to the likely spin temperature  $T_s$ , so that the emission is optically thin. In this limit, the column density  $N_{\text{HI}}$  derived directly from  $W_{\text{HI}}$  is that corresponding to an infinite spin temperature:

$$N_{\text{HI}}(\infty)/C = \int T_b \, dv \equiv W_{\text{HI}}, \quad (1)$$

where the conversion factor  $C = 1.823 \times 10^{18} \text{ cm}^{-2} (\text{K km s}^{-1})^{-1}$  and the integral is over the velocity range specific to a given component. This can be carried out for each spectrum in the data cube, producing a column density map for each of the chosen components. For optically thin emission, this is of course accomplished equivalently by summing channel maps.

We have made  $W_{\text{HI}}$  maps for each GHIGLS field using the velocity cuts in Table 2. Representative maps of  $W_{\text{HI}}$  are shown in Figure 5 for the three velocity components in NEP.

### 6.1. $N_{\text{HI}}$

The quantity  $W_{\text{HI}}$  is a direct observable. Computation of maps of column density  $N_{\text{HI}}$  with allowance for the effects of optical depth is discussed in Appendix C. For the low column densities characteristic of most GHIGLS fields, the corrections are small and so the  $W_{\text{HI}}$  maps scaled by  $C$  are very close to those shown as  $N_{\text{HI}}$  in [Planck Collaboration XXIV \(2011\)](#) for many of the GHIGLS fields, aside from cropping, gridding differences (Section 3.2), and the effect the latter has on the baseline removal. In the results below and on the GHIGLS archive  $N_{\text{HI}}$  has been calculated assuming  $T_s = 80 \text{ K}$  (Equation (C2)). On the archive we have made available FITS files of  $N_{\text{HI}}$  maps for each field. Each file is a cube with five planes (0 to 4) corresponding to the velocity components HVC, IVC, and LVC and in addition IVC+LVC and HVC+IVC+LVC, respectively. We note that all of these maps are in units  $10^{19} \text{ cm}^{-2}$ .

For each component map of the GHIGLS fields, Table 3 gives the mean  $N_{\text{HI}}$ , the lower and upper ends of the range of  $N_{\text{HI}}$  as defined by the 0.1% and 99.9% percentiles, and the uncertainty  $\sigma_{N_{\text{HI}}}$ .

Our estimates of  $\sigma_{N_{\text{HI}}}$  in the first of two columns are derived from differences in repeat observations. Where only single observations are available,  $\sigma_{N_{\text{HI}}}$  is the summation in quadrature of noise, baseline, stray radiation, and scaling uncertainties ([Boothroyd et al. 2011](#)). In Appendix D we present a complementary assessment of the uncertainties in  $N_{\text{HI}}$ , evaluating a second estimate of  $\sigma_{N_{\text{HI}}}$  with a power spectrum analysis (Appendix D.2). These values, in the second of the two columns, are in good agreement with those from the first approach. Uncertainties that could arise from correction for opacity of the line are discussed in Appendix C.

In the tabulated units of  $10^{19} \text{ cm}^{-2}$  the mean column density in LVC ranges from 3.2 in UM1 to 62.3 in HS0624; in IVC, from 0.8 in MRK290 to 14.4 in NEP; and in HVC, from undetectable to 0.02 in LOOP4, to 0.1 in UM2M, and to 6.2 in MC. Summing these, the mean total column density  $N_{\text{HI}}$  ranges from 5.6 in UM2M to 67.4 in HS0624.

Even for the low column densities typical of the

**Table 3**  
Characteristics of  $N_{\text{HI}}$  Component Maps (in  $10^{19} \text{ cm}^{-2}$ )

Name	LVC					IVC					HVC				
	$\langle N_{\text{HI}} \rangle$	$N_{\text{HI}}$	Range <sup>1</sup>	$\sigma_{N_{\text{HI}}}$ <sup>2</sup>		$\langle N_{\text{HI}} \rangle$	$N_{\text{HI}}$	Range	$\sigma_{N_{\text{HI}}}$		$\langle N_{\text{HI}} \rangle$	$N_{\text{HI}}$	Range	$\sigma_{N_{\text{HI}}}$	
MC	6.6	3.8	11.4	0.2	0.1	7.1	4.4	13.2	0.1	0.1	6.2	0.0	21.2	0.4	0.3
BOOTES	7.0	5.2	11.4	0.2	0.1	3.9	1.3	12.1	0.2	0.1	0.2	0.0	1.9	0.1	0.1
Necklace	4.5	3.7	5.6	0.1	0.1	4.4	2.6	5.9	0.2	0.1	...	...	...	...	...
OX3	10.9	7.4	15.9	0.4	0.4	1.6	0.0	4.4	0.4	0.5	1.6	0.0	7.6	0.4	0.7
N1	6.3	4.2	14.3	0.2	0.2	3.1	1.5	15.1	0.2	0.1	3.2	0.0	14.2	0.2	0.2
G86	11.0	4.5	25.1	0.1	0.1	8.0	1.3	37.3	0.2	0.1	0.4	0.0	2.9	0.1	0.1
FLS	17.6	11.9	26.9	0.4	0.2	4.2	2.0	9.2	0.4	0.3	2.0	0.0	7.5	0.4	0.3
MRK290	10.0	7.0	18.8	0.4	0.3	0.8	0.0	9.6	0.2	0.1	4.1	0.0	14.2	0.5	0.3
DRACO	6.5	4.6	16.3	0.1	0.1	11.9	4.2	35.4	0.2	0.2	3.7	0.2	16.0	0.4	0.3
GROTH	6.5	4.8	13.4	0.3	0.2	3.1	0.8	4.7	0.2	0.1	0.6	0.0	3.3	0.3	0.2
NEP	25.9	12.5	56.6	0.3	0.3	14.4	2.7	56.7	0.2	0.2	1.4	0.0	9.3	0.4	0.3
UMIN	52.0	33.4	67.9	0.5	0.4	6.1	3.5	13.0	0.2	0.2	2.3	0.2	11.7	0.4	0.2
POL	56.5	15.8	97.3	0.9	0.5	10.3	4.1	21.0	0.5	0.3	0.4	0.0	5.0	0.6	0.3
POLNOR	35.1	8.8	84.3	0.4	0.4	7.8	1.8	16.9	0.4	0.3	0.2	0.0	8.0	0.6	0.2
MRK205	23.4	9.3	57.2	0.4	0.3	5.0	1.6	13.4	0.4	0.2	0.2	0.0	9.9	0.6	0.2
DFN	4.4	2.0	6.5	0.4	0.2	6.9	4.0	10.0	0.4	0.3	2.6	0.0	9.7	0.3	0.3
SP	6.2	3.8	12.6	0.2	0.2	3.7	1.1	9.6	0.2	0.2	1.9	0.0	9.3	0.3	0.2
UM1	3.2	1.0	6.1	0.5	0.4	13.2	3.8	38.4	0.4	0.4	1.8	0.0	12.9	0.4	0.3
SPIDER	19.9	6.2	69.9	0.3	0.3	7.3	2.1	16.9	0.3	0.3	0.2	0.0	4.2	0.2	0.2
SPC	28.0	9.9	83.7	0.5	0.3	2.6	0.2	10.9	0.2	0.2	0.8	0.0	25.9	0.4	0.2
1H0717	32.4	21.0	70.8	0.5	0.4	3.5	0.9	18.6	0.4	0.2	0.7	0.0	12.1	0.5	0.2
UMA	27.5	10.2	74.4	0.4	0.3	9.4	3.7	24.2	0.4	0.2	0.9	0.0	31.6	0.6	0.2
HS0624	62.3	31.5	109.0	0.5	0.8	2.6	0.7	6.6	0.2	0.2	2.5	0.0	9.3	0.4	0.3
UM3	24.0	4.5	59.7	0.4	0.3	6.6	1.7	19.7	0.3	0.3	0.4	0.0	6.0	0.4	0.2
09A079	4.1	2.4	7.8	0.5	0.2	1.6	0.6	3.0	0.3	0.1	0.3	0.0	2.0	0.4	0.2
UM2M	3.3	1.4	7.2	0.4	0.3	2.2	0.4	6.2	0.3	0.2	0.1	0.0	1.9	0.3	0.1
MS0700	49.8	30.0	76.5	0.5	0.4	2.3	0.7	6.5	0.4	0.2	...	...	...	...	...
UMAEAST	31.4	17.7	55.3	0.4	0.3	9.7	2.7	23.4	0.4	0.3	2.9	0.0	31.2	0.7	0.4
LOOP4	34.5	22.7	47.7	0.4	0.4	8.7	2.0	17.7	0.4	0.3	0.02	0.0	3.5	0.6	0.2
NGC3310	5.8	2.1	16.8	0.3	0.2	4.1	1.5	7.7	0.3	0.2	0.5	0.0	2.4	0.4	0.2
MRK9	43.9	25.1	67.6	0.4	0.3	2.5	0.6	9.0	0.2	0.1	...	...	...	...	...
AG	5.2	2.6	11.8	0.3	0.2	9.5	4.3	16.7	0.2	0.1	3.9	0.0	28.4	0.2	0.2
SUBA	13.9	11.4	17.2	0.3	0.3	6.8	3.9	11.1	0.4	0.3	1.2	0.0	8.9	0.9	0.6
MBM23	57.0	31.1	89.8	0.5	0.5	8.2	3.7	18.6	0.3	0.2	...	...	...	...	...
091346A	12.9	9.3	17.7	0.3	0.3	1.9	0.7	4.7	0.4	0.3	0.2	0.0	1.5	0.3	0.1
MRK421	8.2	4.7	14.4	0.4	0.3	6.7	2.4	23.0	0.4	0.2	...	...	...	...	...
CDFS	5.6	4.0	9.7	0.3	0.4	0.8	0.2	2.8	0.2	0.2	0.2	0.0	3.5	0.3	0.3

<sup>1</sup> The two columns give the lower and upper ends of the range of  $N_{\text{HI}}$  as defined by the 0.1% and 99.9% percentiles of values in the map. Negative  $N_{\text{HI}}$ , which shows up at a level equivalent to the  $N_{\text{HI}}$  noise in faint HVC fields, is excluded in this calculation.

<sup>2</sup> First column: The uncertainty  $\sigma_{N_{\text{HI}}}$  is calculated from repeat observations where available (Table 1), or from estimates of noise in the line emission, baseline, stray radiation, and scaling uncertainties following Boothroyd et al. (2011). Second column: Complementary calculation from power spectrum analysis (Appendix D.2).

GHIGLS fields the data are of high sensitivity, with noise much less than the range of  $N_{\text{HI}}$  within the component maps. Those with the highest range of  $N_{\text{HI}}$  are the most useful for correlating with dust maps, because the morphological match will be better defined statistically.

To identify possible issues in data calibration and reduction, GBT ACS data in a few of the targeted GHIGLS fields are compared to data from a new generation of wide-area H I surveys, in the north EBHIS (Appendix E) and in the south GASS (Appendix F). As shown by Boothroyd et al. (2011), GHIGLS data agree well with the LAB H I survey data, in scale to within a few percent. We find that the agreement with EBHIS data is equally good. A more limited comparison with GASS reveals a calibration difference of about 6%. We note that comparison of GBT 21-cm values of  $N_{\text{HI}}$  with those derived from measurement of Ly $\alpha$  absorption toward high-latitude quasars are in good agreement, in the ratio  $1.00 \pm 0.11$  (Wakker et al. 2011).

## 7. ANGULAR POWER SPECTRUM OF $N_{\text{HI}}$

The two-dimensional angular power spectrum of a map (image of the sky)  $f(x, y)$  is the square of the modulus

of the Fourier transform  $\tilde{f}(k_x, k_y)$  where  $k$  is the spatial frequency (wavenumber) in the Fourier plane (Miville-Deschênes et al. 2007):

$$P(k_x, k_y) = |\tilde{f}(k_x, k_y)|^2. \quad (2)$$

We apodize the image  $f(x, y)$ , from which the median is removed, with a cosine function along its boundary prior to the Fourier transform operation in order to reduce edge effects, which otherwise produce a centered cross in the  $P(k_x, k_y)$  image (Miville-Deschênes et al. 2002). In practice, apodizing over five pixels at each edge is normally sufficient.

The collapsed one-dimensional power spectrum  $P(k)$  is the azimuthal average of  $P(k_x, k_y)$  on a series of annuli of constant  $k = (k_x^2 + k_y^2)^{1/2}$ . Uncertainties are assigned based on the standard deviation of the mean within each of these annuli. If the above-mentioned cross is problematic, then adopting the median rather than the average is an effective alternative; in fact to be conservative we always adopted the median. To mitigate against these effects further, the data point at the lowest  $k$  was excluded in the analysis below.

The dots in Figure 6 illustrate the basic anatomy of

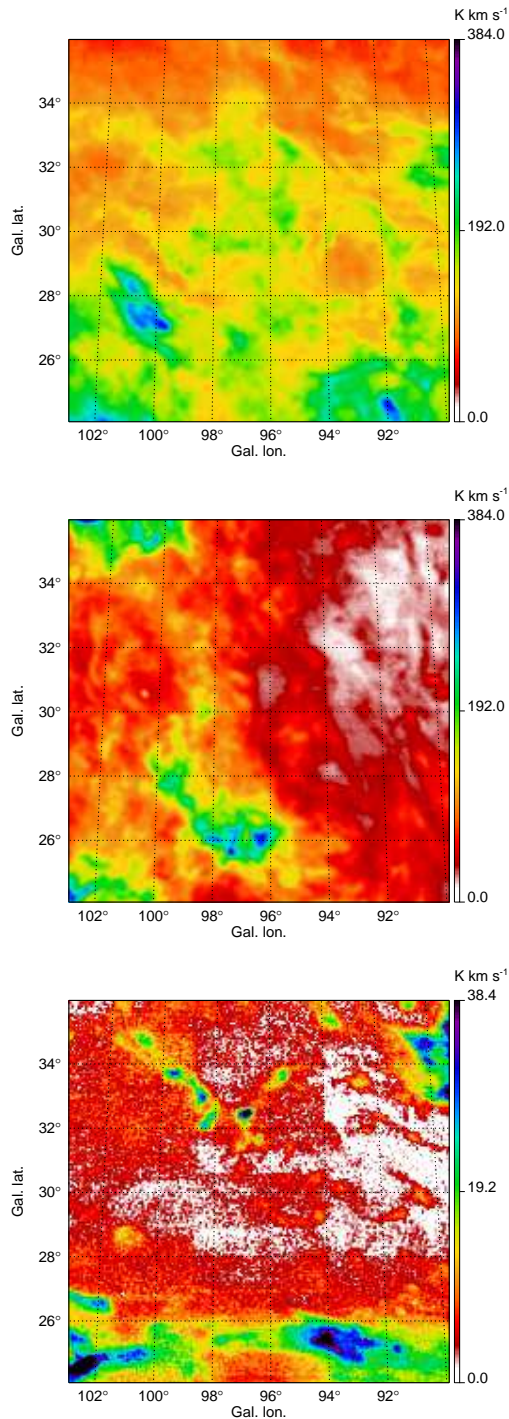


**Figure 5.**  $W_{\text{HI}}$  maps for NEP (upper, middle, lower: LVC, IVC, HVC). Note that the range in the colorbar in the HVC map is a factor of ten smaller so that the noise level is apparent in the map.

the power spectrum of our data. At small  $k$  (large spatial scales in the map),  $P(k)$  roughly follows a power law:  $P_o (k/k_o)^\gamma$ , where  $P_o$  is the amplitude of the power spectrum at some representative scale  $k_o$  and  $\gamma$  is the scaling exponent. The exponent is alternatively called the spectral index or the slope (in a log–log representation as in Figure 6). The size of the exponent and its variations from one type of map to another provide insight into the turbulent structure of the ISM (Hennebelle & Falgarone

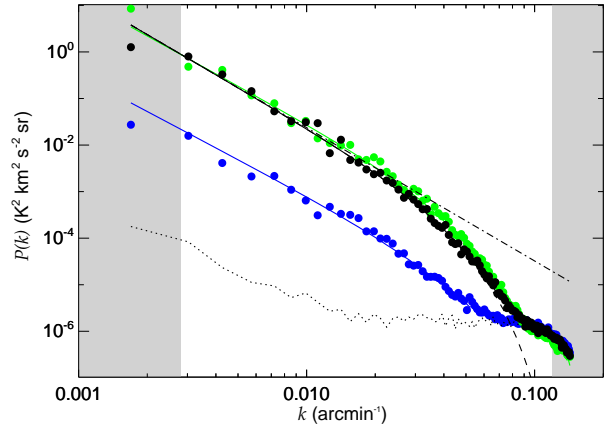


**Figure 6.** Median power spectra of component maps of  $N_{\text{HI}}/C$  in the NEP (black: LVC; green: IVC; and blue: HVC). Overlaid are fits (solid lines) to the model in Equation (5). As shown only for the case of LVC, this model consists of a power law (dash dot line), modified by the GBT beam (resulting in dashed line), plus the scaled noise template (dotted line). Shaded regions define ranges of  $k$  excluded from the fit.

2012).

At large  $k$  the power law is modified by the effect of the point spread function (beam) of the telescope and the noise. For a symmetrical Gaussian beam  $\phi$  described in one spatial dimension by its FWHM we have

$$\phi(x) = \exp\left(-\frac{x^2}{2\sigma^2}\right) \text{ and } \tilde{\phi}(k) = \exp\left(-\frac{k^2}{2\sigma_k^2}\right), \quad (3)$$

where the dispersion  $\sigma = \text{FWHM}/(2\sqrt{2\ln 2})$  is related to  $\sigma_k$  by the Fourier relation  $\sigma_k = 1/(2\pi\sigma)$ . Above  $k \approx 0.04$ , where spatial scales are comparable to the size of the GBT beam, the intrinsic  $P(k)$  is reduced multiplicatively by  $\tilde{\phi}^2(k)$ . This can be seen in the power spectra in Figure 6. At even higher  $k$ , the noise dominates; the distinctive shape of the noise power spectrum is discussed in Appendix D.2.

We have investigated the effect of the asymmetrical beam. For the range of spatial scales sampled before the signal disappears into the noise, the optimal beam size is 9.24 when treated as a Gaussian. As an alternative, starting with an image of the effective beam calculated for our modified Bessel function gridded data cubes (Section 3.2), we computed from its power spectrum the azimuthally averaged  $\tilde{\phi}^2(k)$ . From our model of the GBT beam we estimate an additional uncertainty

$$\delta P(k) = b P(k) (1 - \tilde{\phi}^2(k)), \quad (4)$$

where  $b$  is an adjustable fractional error that we set to 0.07. This is added in quadrature to the uncertainty derived for each annulus of constant  $k$ . While it is only an approximation,  $\delta P$  has the desired effect of assigning lower weight to data strongly affected by the beam and still fitting the noise adequately. The parameters derived from the fits below are not sensitive to the precise choice of  $b$ . We also mitigated against further uncertainty by excluding data above a value  $k_{\text{max}}$ ; again the results below are not sensitive to the precise value so long as the noise can be adequately assessed, and we adopted  $0.12 \text{ arcmin}^{-1}$ .

### 7.1. Power Spectrum Model

The computed power spectrum is fit to data in the restricted range of  $k$  with a parameterized model consisting of a power law, modified by the beam, plus noise:

$$P_{\text{model}}(k) = \tilde{\phi}^2(k) P_o (k/k_o)^\gamma + \eta N(k). \quad (5)$$

The origin of the noise model,  $N(k)$ , scaled by fitting factor  $\eta$ , is discussed in Appendix D.2. The best-fit parameters are found using the above uncertainties as weights in the IDL routine `mpfit.pro` (Markwardt 2009). The derived model is plotted in Figure 6. We also inspected a plot of  $P(k)/P_{\text{model}}(k)$  to verify that there was no bias hidden by the logarithmic display.

For the three component maps of  $N_{\text{HI}}$  of the NEP field the model fit to the data (see Figure 6) yields exponents  $-2.86 \pm 0.04$ ,  $-2.69 \pm 0.04$ , and  $-2.59 \pm 0.07$  for LVC, IVC, and HVC, respectively. The uncertainties cited are the formal  $1\sigma$  errors from the fits and do not include any systematic uncertainties. From extensive testing of alternative choices in the fitting analysis, we estimate that systematic uncertainties of the exponent are of order 0.1 for the LVC map and probably somewhat smaller for the IVC and HVC maps. We also found that relative differences between the exponents for different components are robust against the systematic effects. The IVC component has a marginally shallower spectrum compared to the LVC component, as can be seen directly from the data in Figure 6.

With respect to the summary by Hennebelle & Falgarone (2012), the exponent for NEP LVC is roughly consistent with the value of  $-2.75$  for H I seen in absorption (Deshpande et al. 2000), but by contrast much shallower than the exponent of  $-3.6$  for H I in emission found by Miville-Deschênes et al. (2003a) in an intermediate latitude field in Ursa Major. The comparison of power spectra component by component among different GHIGLS fields is an interesting topic taken up in a forthcoming paper.

The values from H I column density can be compared to those from dust emission maps, for example the value of  $-2.9$  for dust calculated for four regions at  $100 \mu\text{m}$  (Gautier et al. 1992). Extending analysis to the entire high latitude sky Miville-Deschênes et al. (2007) found a median  $-2.93$  with considerable dispersion (0.3) from region to region and a trend of flattening for fainter regions. A value of  $-2.7 \pm 0.1$  was obtained for dust mapped in the Polaris flare with *Herschel*/SPIRE  $250 \mu\text{m}$  and IRIS  $100 \mu\text{m}$  (Miville-Deschênes et al. 2010). The *Planck* 857 GHz mask-differenced power spectrum (Planck Collaboration XVI 2014), characterizing Galactic dust in the intermediate latitude sky, has an exponent reaching  $-2.6$  asymptotically at high  $\ell$  multipoles, in the range relevant to our analysis.

We note that the exponent for the *Planck* 353 GHz EE and BB polarized dust power spectra in the intermediate latitude sky (Planck Collaboration Int. XXX 2014) is quite similar,  $-2.42$ , even though these spectra depend additionally on the linkage of the statistical properties of density and magnetic field geometry.

A detailed discussion of the relationship between the power spectra of  $N_{\text{HI}}$  maps and dust emission maps of the same GHIGLS fields will also be presented in the forthcoming paper.

### 8. GAUSSIAN DECOMPOSITION OF LINE PROFILES

With a goal of understanding the physical conditions and velocity structure in the diffuse regions where these spectra originate, we have analysed the H I line profiles by decomposition into a series of Gaussian functions using a method similar to that of Haud (2000), details of which can be found in another forthcoming paper (Blagrave, K. et al. 2015, in preparation). Each spectrum is fit within the noise with multiple Gaussian components, with Gaussian parameters amplitude, centroid velocity, and FWHM (or dispersion  $\sigma$ ). Each spectrum is fit individually independent of its neighbors, but further iterative modifications could include information from neighboring solutions, resulting in a more spatially coherent set of components.

As described further below (see also Blagrave, K. et al. 2015, in preparation), using various simulations based on Saury et al. (2014) we have found that the decomposition distinguishes effectively different parcels of gas at different temperatures. From simulated IVC plus LVC cubes (as in Section 5), we have also examined various sets of two-dimensional histograms of the Gaussian parameters in order to differentiate IVC and LVC gas.

#### 8.1. Distributions of Recovered Gaussian Parameters

We illustrate the results on GHIGLS data using the NEP field for which the average number of Gaussians fit to a given spectrum is 4.8. Figure 7 shows a pair of two-dimensional histograms of the parameters for all Gaussian components in the FWHM–centroid and FWHM–amplitude planes. The FWHM–centroid histogram (left) typically reveals what can be called “pillars,” vertically-aligned features with an approximately constant centroid over a range of FWHM values. A particularly distinct example of such a pillar appears at  $v \sim 0 \text{ km s}^{-1}$  in the range of the NEP LVC gas. In other GHIGLS fields, pillars can be seen at other LVC and IVC centroid velocities, with varying degrees of contrast.

There is a sharp decrease in the number of lines as the recovered FWHM decreases below  $2 \text{ km s}^{-1}$  (e.g., Figure 7, right), similar to what has been found for both the LAB (Haud & Kalberla 2007) and GASS (Kalberla & Haud 2015) surveys: H I emission lines narrower than FWHM  $2 \text{ km s}^{-1}$  are rarely found. A FWHM of  $2 \text{ km s}^{-1}$  could arise as the thermal line width of 100 K gas or might reflect the contribution of turbulence if the gas is even colder. The few components with FWHM  $< 1 \text{ km s}^{-1}$  are unphysical, the result of the automated fitting routine attempting to improve the model by fitting Gaussians to rare remaining noise spikes.

There are a few other features in three-dimensional parameter space that we have identified as unphysical Gaussian components that arise because of the limitations of automated unconstrained Gaussian fitting routines. For example, a number of features with very low  $W_{\text{HI}}$  improve the model by fitting Gaussians to residual baselines. These can be excluded in Figure 7 right; any component with  $W_{\text{HI}} < 1.0 \text{ K km s}^{-1}$  is below the detection limit as determined by the error analysis in Boothroyd et al. (2011) and uncertainties in Table 3.

At the other extreme, there are very broad components with low amplitude that show up consistently with centroids between LVC and IVC in the FWHM–centroid

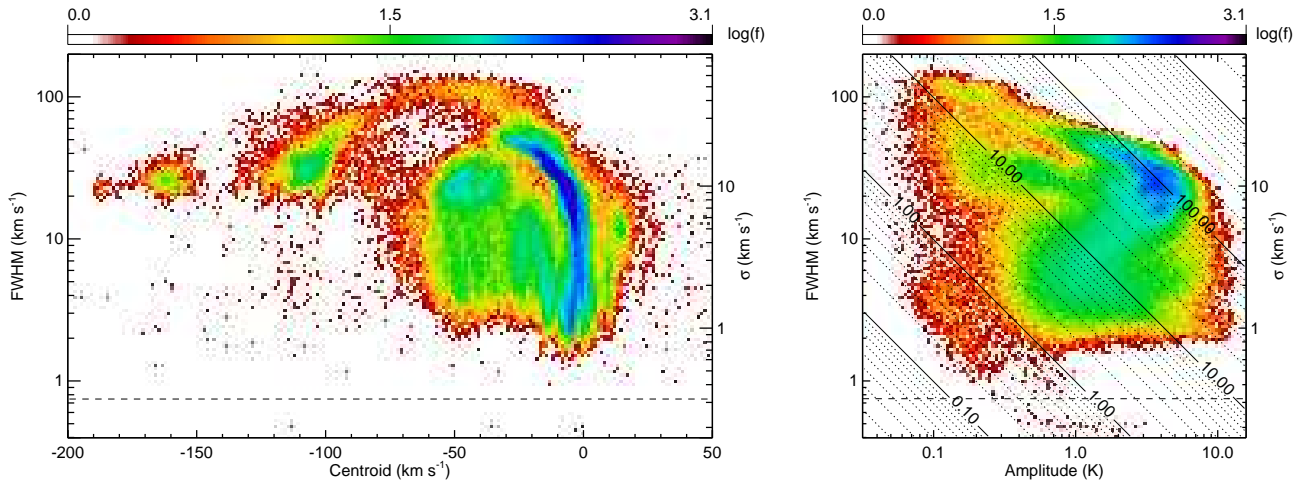


**Figure 7.** Histograms with respect to parameters of Gaussian components fit to spectra in the NEP field. The number of components in each two-parameter bin,  $f$ , is shown on a logarithmic scale quantified by the colorbar. Left: FWHM–centroid histogram. Components of the LVC gas with centroids near  $0 \text{ km s}^{-1}$  have a large range of FWHM and the ridge in the histogram forms a distinctive vertical “pillar.” At large FWHM the ridge in the histogram “arches” toward lower centroid velocities because of components with unphysically large FWHM fit to low amplitude emission from both IVC and LVC gas (see text). Right: FWHM–amplitude histogram. Lines of constant  $W_{\text{HI}}$  ( $\text{K km s}^{-1}$ ) are shown as solid and dotted diagonal lines. Components with  $\text{FWHM} < 1 \text{ km s}^{-1}$  (dashed line) are flagged as unphysical; these typically have low  $W_{\text{HI}}$ . Any component with  $W_{\text{HI}} < 1.0 \text{ K km s}^{-1}$  is below the noise limit.

histograms (Figure 7 left), creating “arches” between the pillars. Similarly, arches of extremely broad components also appear in the FWHM–centroid histogram with centroids between LVC and HVC. We have demonstrated that these too are unphysical, as follows. As in Section 5, we used the hydrodynamical simulations of Saury et al. (2014) to create an IVC plus LVC cube. Although this cube contains no intrinsic very broad components, we found on Gaussian decomposition (Blagrave, K. et al. 2015, in preparation) that such very broad components nevertheless do arise, again appearing at intermediate velocities between the LVC and IVC pillars in the FWHM–centroid histogram. In the simulation and actual data these are artifacts of the Gaussian fitting routine, a result of fitting a single Gaussian to a merger of two (or more) weaker, narrower Gaussian components.

### 8.2. Maps of $N_{\text{HI}}$ for Components with Different Line Widths

The aforementioned LVC, IVC, and HVC velocity-selected components would be closely related to the Gaussian components forming vertical pillars within a range of centroid velocity in FWHM–centroid histograms. For example we would select Gaussian components as LVC if their centroids fall in the velocity range for LVC from Table 2, which for NEP is  $-20.5 < v < +47.9 \text{ km s}^{-1}$ .

These histograms suggest a possible new complementary direction for the subdivision of a cube into components on the basis of distinctive FWHM. As mentioned above narrow and broad components are commonly associated with two phases of the diffuse neutral atomic ISM: the CNM and the WNM, respectively. Analysis of histograms from all of the GHIGLS Gaussian components suggests that the natural division  $\text{FWHM}_d$  between narrow and broad Gaussian components for the LVC emission occurs at about  $7.1 \text{ km s}^{-1}$ . With this division we can make  $N_{\text{HI}}$  maps corresponding to CNM and WNM by summing up the contributions from the appropriate

components. To allow for uncertainties introduced by the Gaussian decomposition model and particularly by a sharp divide at  $\text{FWHM}_d = 7.1 \text{ km s}^{-1}$ , we have employed a Monte Carlo approach to produce and average  $\sim 100$  versions of the map using  $\log \text{FWHM}_d$  drawn from a normal distribution with a  $1\sigma$  dispersion of 0.05 dex about the indicated mean.

The CNM–WNM separation using the Gaussian component approach can be tested using simulations in which the true results are known *a priori* because the gas temperature is known. For example, we have studied (Blagrave, K. et al. 2015, in preparation) a simulation from Saury et al. (2014) for which  $\zeta = 0.2$ ,  $v_s = 12.5 \text{ km s}^{-1}$ , and  $n_0 = 1.0 \text{ cm}^{-3}$ , resulting in  $f_{\text{CNM}} \sim 0.29$ . As we did above for the GHIGLS observations, in that work we selected a division in FWHM based on the distribution of Gaussian components for the simulation, in that case finding  $\text{FWHM}_d = 4.5 \text{ km s}^{-1}$ . This results in  $f_{\text{CNM}} \sim 0.32$ , consistent with the actual  $f_{\text{CNM}}$  for the simulation. This test also showed reasonable agreement between narrow and broad-component column density maps created from the Gaussian components and corresponding maps created from gas in known temperature ranges.

The CNM  $N_{\text{HI}}$  map thus made from the selection of Gaussian components for NEP LVC is shown in Figure 8, upper, as  $N_{\text{HI}}/C$ . The CNM map has a low column density compared to the total LVC but also highlights the filamentary structure running roughly diagonally across the field. The fraction of CNM in the LVC of NEP by column density is  $f_{\text{CNM}} \sim 0.08$ , reflecting the dearth of narrow Gaussian components identified along many lines of sight in the NEP. We note that the CNM fraction by mass could be different, depending on the relative distances of the CNM and WNM gas. This value of  $f_{\text{CNM}}$  can be compared to those obtained directly from absorption line spectra. Heiles & Troland (2003) found a global ratio of CNM to total  $N_{\text{HI}}$  of 0.39 for the Arecibo sky. This is an upper limit for the mass fraction of CNM be-

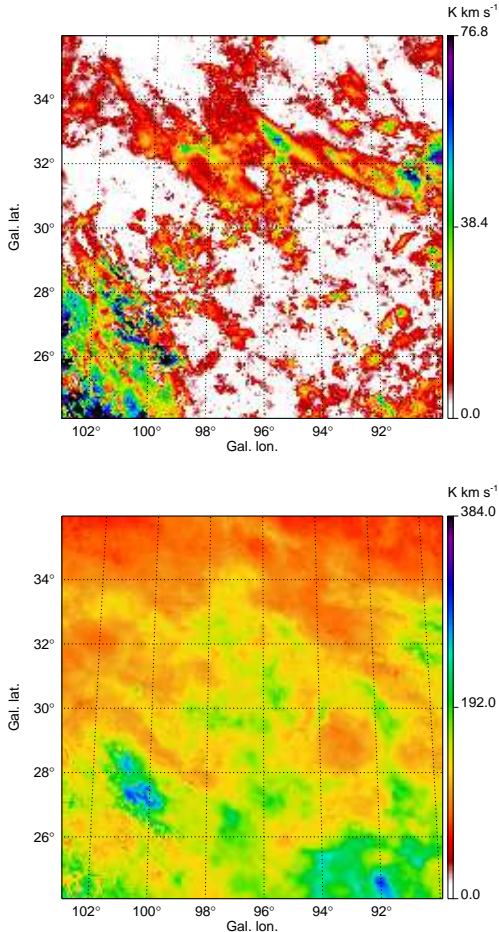


**Figure 8.** Column density maps for NEP for gas in the LVC range in units  $N_{\text{HI}}/C$  from Equation (C2) after Gaussian decomposition of the line profiles. Upper: Column density from narrow components ( $\text{FWHM} < 7.1 \text{ km s}^{-1}$ ) and assuming  $T_s = 80 \text{ K}$ . Note that the range in the colorbar is a factor of five smaller than for the map below. This map can be interpreted as from the CNM. Filamentary structure is seen with a roughly diagonal orientation as in individual channel maps (cf. Figure 3, upper right). Lower: Column density map obtained by subtracting the above CNM map from the map of the total LVC component in Figure 5, upper. This is interpreted as being from the WNM and in this field is very similar to the total.

cause of the systematic difference in distance between the CNM and WNM. Likewise, Dickey et al. (2009) found a fraction  $f_{\text{CNM}} \sim 0.15 - 0.20$  for the outer Galaxy. The result for CNM in the LVC range in NEP is therefore lower than these global values.

We note that the observed low  $f_{\text{CNM}}$  in NEP can be described well with appropriate tuning of the parameters in the Saury et al. (2014) simulations. For example, some simulations with  $\zeta = 0.3$ ,  $v_s \sim 15 \text{ km s}^{-1}$ , and  $n_0 = 1.0 \text{ cm}^{-3}$  result in  $f_{\text{CNM}} = 0.11$ .

Also shown in Figure 8, lower, is the WNM  $N_{\text{HI}}$  map. Because of the complications of the unphysical arches at high FWHM, this has been produced simply by subtracting the CNM map from that of the total LVC emission (Figure 5, upper). The WNM map is quite similar to the total LVC map, given the low  $f_{\text{CNM}}$ .

### 8.3. Power Spectra of Maps of $N_{\text{HI}}$ for Components with Different Line Widths

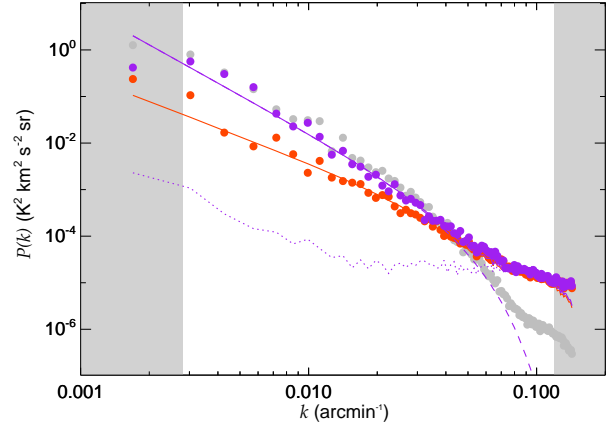


**Figure 9.** Power spectrum of  $N_{\text{HI}}/C$  of the NEP as in Figure 6, but for LVC emission separated into CNM (red) and WNM (purple) components (Figure 8). Overlaid as gray circles is the power spectrum for the total LVC  $N_{\text{HI}}/C$  from Figure 6. The Gaussian decomposition introduces an additional uncharacterized noise component in the  $N_{\text{HI}}$  maps near the pixel scale, reflected at high spatial frequencies in the power spectrum above the modelled beam turnover (compare the purple and gray points); see text.

The power spectra of the  $N_{\text{HI}}$  maps of the LVC CNM and WNM components for NEP are shown in Figure 9. The WNM component accounts for most of the  $N_{\text{HI}}$  of the LVC emission and so its power spectrum is similar to that of the total LVC emission in Figure 6. The CNM spectrum has less power overall and a shallower dependence on  $k$ .

Note that the shape of these power spectra at high  $k$  (Figure 9) is markedly different from that of the integrated  $W_{\text{HI}}$  maps (Figure 6). Despite attempts that can be made to keep solutions smoothly varying from pixel to pixel, the Gaussian fitting introduces an additional uncharacterized noise contribution near the pixel scale, which is reflected in the component  $N_{\text{HI}}$  maps and propagates to a larger noise in the power spectrum at high  $k$  above the modelled beam turnover of the signal. In the model fitting we allow for this by the simple device of increasing the beam uncertainty parameter in Equation 4 to  $b = 0.3$ , which in effect gives lower weight to the many data values at the highest  $k$  where noise now dominates.

The model fits to the LVC WNM and CNM component maps (see Figure 8) yield exponents of  $-2.7 \pm 0.1$  and  $-1.9 \pm 0.1$ , respectively. The exponent for the WNM component map is close to the exponent for the total LVC emission,  $-2.86 \pm 0.04$  (Section 7.1), within the systematic errors, as expected because this component contains most of the mass. However, the power spectrum for the CNM component map is clearly shallower than for the WNM, a differential result that is robust against systematic effects of how the model is fit. The significantly flatter spectrum found for the CNM map quantifies what can be foreseen readily in the maps themselves: the CNM map has more high-contrast small angular scale filamentary structure than the WNM map.

Such a shallow dependence in a narrow-line component is not unexpected. The spectrum of the density on two-dimensional slices through the simulated cube used for the test in Section 8.2 has an exponent of  $-1.3$ , a much shallower dependence than from the Kolmogorov exponent of  $-8/3$ . Thus the spectrum of the three-

dimensional density would be  $-2.3$  and furthermore this would be the exponent of the column density map of the cube (Miville-Deschênes et al. 2003b).

Saury et al. (2014) also expect from their simulations of thermally bistable gas that the CNM power spectrum will be shallower than for the warm gas. Indeed, power spectra of  $N_{\text{HI}}$  maps produced from these simulations by selecting on the temperature of the gas (Blagrave, K. et al. 2015, in preparation) have much shallower power spectra for the CNM ( $\sim -1.9$ ) as compared to the WNM ( $\sim -2.9$ ).<sup>13</sup>

In addition to small scale structure corresponding to enhanced concentration of H I in the CNM, there are also possible effects from cold neutral gas becoming molecular and thus leaving structure in the remaining H I, albeit probably with lower contrast. The molecular transition is not modeled in these particular simulations.

The CNM angular power spectra described here for both the NEP LVC range and the simulated data are significantly shallower than anything noted previously for H I emission, H I absorption, CO line emission, or dust emission (see Figure 10 in Hennebelle & Falgarone 2012).

#### 9. RELATIONSHIP OF H I CNM STRUCTURE TO THE ORIENTATION OF THE MAGNETIC FIELD

In Section 4 we commented on the striking filamentary structures in the LVC channel maps of NEP that cross the region roughly diagonally (lower right to upper left). See the channel map in Figure 3. These features are fairly narrow in line width (present over only a few adjacent channel maps, as is evident in the movie of the cube) and so imprint on the  $N_{\text{HI}}$  map made from the narrow Gaussian components (Figure 8, upper). As is illustrated in Figure 10, this filamentary H I structure in the condensed CNM in NEP is aligned roughly parallel to the direction of the Galactic magnetic field projected on the plane of the sky as inferred from the *Planck* 353 GHz thermal dust polarization map (Planck Collaboration Int. XIX 2015).

This relative orientation is in accord with the recent finding that the magnetic field tends to be oriented parallel to the elongation of filamentary dust structures in both the high latitude sky (Planck Collaboration Int. XXXII 2014) and in nearby Gould Belt molecular clouds (Planck Collaboration Int. XXXV 2015). Such a systematic tendency in relative orientation is important for understanding the observed power in B-mode relative to E-mode dust polarization (Planck Collaboration Int. XXXVIII 2015).

It is also interesting to note that the Cygnus spur end of Loop III seen in synchrotron emission also crosses NEP on the same diagonal and that the polarization of the synchrotron emission indicates that the magnetic field is parallel to the loop (Planck Collaboration XXV 2015). Thus in NEP the predominant orientation of the field revealed by thermal dust and synchrotron polarization is similar.

The observed *Planck* polarization arises from dust not just in the CNM gas, but in the WNM gas within which

<sup>13</sup> Another way to generate such a shallow power-law dependence is with cold and supersonic gas, as seen in simulations of isothermal high Mach number flows (e.g., Kim & Ryu 2005); however, these conditions seem less relevant to the general interstellar medium than those in the simulations of Saury et al. (2014).

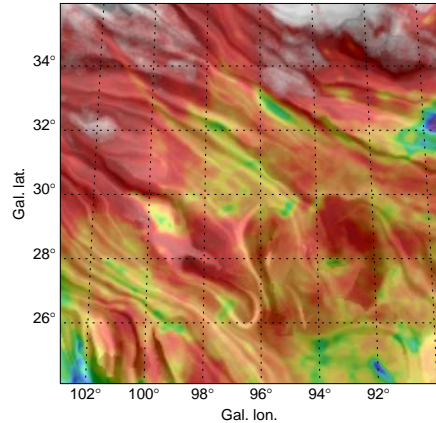


**Figure 10.** View of the magnetic field measured by *Planck* overlaid on a map of  $N_{\text{HI}}$  from selected LVC gas in NEP. The “drapery” pattern, produced using the line integral convolution (LIC, Cabral & Leedom 1993), indicates the orientation of magnetic field projected on the plane of the sky, orthogonal to the observed dust polarization (Planck Collaboration Int. XIX 2015). The colors represent  $N_{\text{HI}}$  integrated over seven channels at the peak of the LVC emission ( $-6.4$  to  $-1.6$   $\text{km s}^{-1}$ ), highlighting the structure of CNM gas. This illustrates how the orientation of the CNM gas filaments tends to follow the magnetic field across the upper part of the image, among several interesting relationships between the gas and the field (see text).

the CNM is embedded. Thus the field orientation highlighted in the CNM structure is more pervasive. (In addition, dust in the IVC contributes to the total emission, with about half the emissivity and perhaps some polarization.) The relationship between gas and magnetic field is quite interesting in its complexity. For example, the field appears to wrap around a depression in the gas emission at  $(l, b) = (93^\circ, 28^\circ)$  (see also the total LVC in Figure 5, upper), suggestive of a bubble. Below that the field appears to wrap around the edge of the enhanced gas emission.

#### 10. CONCLUSIONS

In this paper we present data from the GBT H I survey, GHIGLS. This deep/sensitive survey covers targeted regions of the intermediate Galactic latitude sky including several with distinctive IVC and/or HVC features.

The data have been calibrated and corrected for stray radiation following Boothroyd et al. (2011). Data for most regions has an rms noise  $\lesssim 100$  mK in a  $0.8$   $\text{km s}^{-1}$  channel. The effect of 21-cm line opacity on the calculated column density  $N_{\text{HI}}$  and various other small sources of uncertainty in the GHIGLS measurements of  $N_{\text{HI}}$  are discussed.

GHIGLS data agree well with the LAB H I survey data, in scale to within a few percent. We find that the agreement with EBHIS data is equally good. A more limited comparison with GASS reveals a calibration difference of about 6%.

We divide the H I emission into components with different velocities and produce  $N_{\text{HI}}$  maps of LVC, IVC, and HVC components. Structure in these maps is quantified by the angular power spectrum modelled with a power law. For the NEP field, the power-law exponent for LVC ( $-2.86 \pm 0.04$ ) is close to that found for dust maps in the intermediate Galactic latitude sky; the exponents for IVC and HVC reveal a marginally flatter power-law be-



havior (exponents  $-2.69 \pm 0.04$  and  $-2.59 \pm 0.07$ , respectively).

We fit the spectral line profiles with multiple Gaussian components to differentiate gas characterized by different line widths, enabling a subdivision into emission by two ISM phases, the WNM and CNM. The CNM map of  $N_{\text{HI}}$  is unique in its angular power spectrum, having a power-law exponent of  $-1.9 \pm 0.1$  for LVC in the NEP field, shallower than seen in any component map but consistent with the power-law exponent of CNM seen in simulations. The flatter power-law behavior reflects more small scale structure associated with this phase.

There is evidence that filamentary structure in the H I CNM gas is aligned with the Galactic magnetic field revealed by *Planck* polarization.

GHIGLS data have already been used productively in a number of Galactic and extragalactic applications and should be interesting for many more. On the GHIGLS archive ([www.cita.utoronto.ca/GHIGLS](http://www.cita.utoronto.ca/GHIGLS)), fully-reduced data cubes, along with movies and  $N_{\text{HI}}$  component maps, are available for inspection and downloading.

We acknowledge support from the Natural Sciences and Engineering Research Council (NSERC) of Canada. We thank the NRAO staff for their outstanding support, in particular G.I. Langston for providing code that was important to the data reduction. We are grateful to Eleonore Saury for making available data cubes from her hydrodynamical simulations and to Daniel Lenz, Peter Kalberla, and the EBHIS team for providing unpublished data cubes from the EBHIS survey. We thank the referee for constructive comments that have led to improvements in this presentation of our results.

## APPENDIX

### A. DATA OBTAINED USING THE GBT SPECTRAL PROCESSOR

As indicated by the notes in Table 1, 11 fields including the central portion of the BOOTES field were observed with the now-retired GBT Spectral Processor (GBT SP). As is the case for the GBT ACS data, these data were collected in in-band frequency-switched mode, except for the FLS field observed with out-of-band frequency switching. The FLS data were regridded from the observed  $0.5 \text{ km s}^{-1}$  spaced channels to the adopted ACS spacing of  $0.807 \text{ km s}^{-1}$ , using a cubic spline interpolation. For the other fields the channel spacing was maintained as observed at  $1.03 \text{ km s}^{-1}$  (for the entire BOOTES data, this was adopted even for the ACS portion). The number of repeats and the resulting emission-free channel noise,  $\sigma_{\text{ef}}$ , are found in Table 1.

We processed the raw GBT SP data following the GBT ACS pipeline described in Section 3.1 and Boothroyd et al. (2011), including the benefit of the improved stray radiation correction over Lockman & Condon (2005). For consistency with the GBT ACS cubes, the spectra were gridded on a  $3/5$  grid using the modified Bessel function.

There is a slightly different calibration unique to the GBT SP because in that era there was a different noise diode in the GBT 21-cm receiver. Therefore, the calibration discussed in Boothroyd et al. (2011), specifically the scaling of  $T_{\text{a}}$  by the factor  $1.024 \pm 0.009$ , is not relevant.

The scaling of  $T_{\text{a}}$  appropriate to the GBT SP data was investigated in two ways. The first approach used archival GBT SP data on the S6 and S8 calibration standards. For these, the  $XX$  and  $YY$  spectra are slightly inconsistent with each other – differing by 5 to 10% – but their average spectrum,  $(XX + YY)/2$ , is reproducible and indicates consistently that the GBT SP measure of the main beam temperature  $T_{\text{b}}$  is 1.05 to 1.08 larger than for the GBT ACS spectra of these calibrators. The second approach compared regions of overlap between spectral cubes made with GBT SP observations with cubes made with GBT ACS observations: the original SP central field in BOOTES with the ACS flanking fields, UM2M with NGC3310, UM2M with 09A079, UM3 with UMA (and LISZTA), and FLS with NEP (see Figure 1). These comparisons indicate overestimates of the same order (1.05 to 1.08). Therefore, in the final pipeline processing the GBT SP  $T_{\text{a}}$  data were scaled using a factor  $0.97 (\pm 0.01)$  instead of 1.024 to bring the GBT SP data onto the same  $T_{\text{b}}$  scale as the GBT ACS data.

### B. ARCHIVAL DATA OBTAINED FOR 09A079 USING THE GBT AUTO-CORRELATION SPECTROMETER

The low column density region within the Lockman Hole is covered in part by the H I survey UM2M using the SP (Appendix A) and an overlapping field 09A079 observed by Grossan et al. (2012) using the ACS (proposal GBT/09A-079). The latter data were obtained to estimate the Galactic dust foreground for studies of the CIBA using a  $160 \mu\text{m}$  map from *Spitzer* and to probe the relation between dust and gas in this very low dust regime. Because of the low column density it is essential to correct the H I spectra for stray radiation before embarking on the science analysis. Therefore, we have reprocessed these ACS data using the pipeline that we developed (Section 3). This cube is available on the GHIGLS archive and we have used it in the LHM mosaic described in Section 3.3. These observations were carried out by mapping several overlapping subfields, some of which involved scans along constant Galactic longitude rather than the more usual constant Galactic latitude. The subfield structure and irregular coverage is not detailed in Table 1, but is imprinted in the noise and weight maps.

### C. OPTICAL DEPTH EFFECTS

A diagnostic warning that an observed H I spectrum might be affected by opacity is if  $T_{\text{b}}$  approaches the (plausible) spin temperature  $T_{\text{s}}$ . In the extreme the line profiles might become flat topped, but that is rarely encountered here. We wish to explore more subtle effects.

In the absence of absorption-line measurements to combine with the emission measurements to distinguish the effects of optical depth  $\tau$  (Strasser & Taylor 2004; Dickey et al. 2009), as is the case for GHIGLS data, it is nevertheless possible to make an estimate of the potential optical depth effects for different assumed  $T_{\text{s}}$ . As a reasonable spin temperature we adopt  $T_{\text{s}} = 80 \text{ K}$  which is the collisional temperature found from intermediate-latitude  $H_2$  observations for column densities near  $10^{20} \text{ cm}^{-2}$  (Gillmon et al. 2006; Wakker 2006). This would be appropriate for CNM. The CNM equilibrium temperature is not constant but depends inversely

on the local density. Estimates of the CNM temperature in the Galactic plane do show lower values (Dickey et al. 2003); however, Heiles & Troland (2003) find that for  $|b| > 10^\circ$  and CNM column densities near  $10^{20} \text{ cm}^{-2}$ , the mass weighted  $T_s$  is 70 K (median) and 108 K (average).

### C.1. Complications in a Multi-phase ISM

Differences among and within individual observed H I line profiles for different lines of sight and their overall complexity are reminders that a single  $T_s$  is naive. The emission is summed over gas in different stable phases of atomic gas with different temperatures, the CNM and WNM, and there could be substantial amounts of warm thermally unstable gas as well (Heiles & Troland 2003; Haud & Kalberla 2007; Hennebelle & Falgarone 2012; Saury et al. 2014). While  $T_s$  for the CNM might be near 80 K,  $T_s$  for the WNM is much higher ( $> 300$  K; Dickey et al. 2009). One could carry out component (phase) separation by line profile decomposition (see Section 8), to segment CNM and WNM and then assign different  $T_s$  in correcting these classes of profile. But even this would not capture the complexities arising from the relative geometries of the gas in different phases.

However, in GHIGLS the highest values of  $T_b$  in the observed profiles are caused by the CNM. We have shown this by making a cube of the CNM gas emission using the Gaussian decomposition method discussed in Section 8. For each voxel we then formed the ratio  $T_b(\text{CNM})/T_b$  and found that the ratio approaches unity for higher  $T_b$ . Because optical depth corrections become important for  $T_b$  comparable to  $T_s$ , which is accentuated in CNM gas where  $T_s$  is low, such high- $T_b$  parts of the profile are most in need of correction, using a  $T_s$  appropriate to CNM.

On the other hand at intermediate latitudes the WNM produces broad profiles that have low  $T_b$  and so the magnitude of a correction even using a  $T_s$  that is inappropriately low will be inconsequential. Therefore, a simple correction using a single  $T_s$  appropriate to CNM might not be unreasonable. That is the approach that is evaluated quantitatively here.

### C.2. Impact on $N_{\text{HI}}$

The actual column density is always larger than the direct line integral  $N_{\text{HI}}(\infty)$  in Equation (1) and within our assumptions is given by

$$N_{\text{H}}(T_s)/C = \int T_s \tau \, dv \quad (\text{C1})$$

$$= T_s \int -\log(1 - T_b/T_s) \, dv \quad (\text{C2})$$

$$= W_{\text{HI}} + 1/(2T_s) \int T_b^2 \, dv + \dots \quad (\text{C3})$$

The first-order correction,  $1/(2T_s) \int T_b^2 \, dv$  from Equation (C3), is quadratic in  $T_b$ . Therefore, the  $T_b^2$  cube, and maps of integrals made from it, reveal where there is sensitivity to optical depth. The form of the first-order correction has the great utility of showing the explicit scaling with  $1/(2T_s)$ , quantifying the importance of an appropriate choice of  $T_s$ .

In Figure 11 we show the first-order correction from Equation (C3) as a function of the optically thin solu-

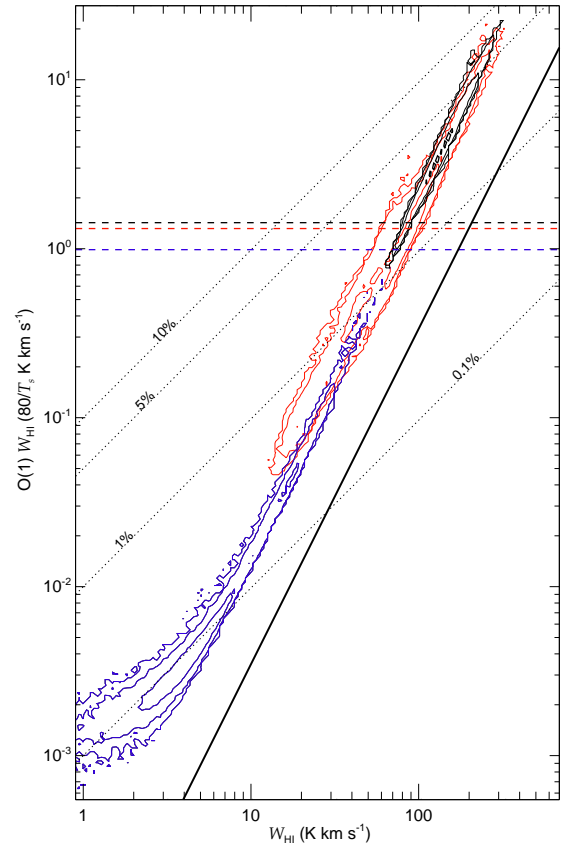


**Figure 11.** Contours of histogram of the first-order correction,  $1/(2T_s) \int T_b^2 \, dv$ , as a function of the optically thin solution  $W_{\text{HI}}$  for NEP, here using  $T_s = 80$  K. Values for the three components are overplotted in different colors: LVC (black), IVC (red), and HVC (blue). A line segment of slope two reveals the approximate quadratic dependence. The unit-slope dotted lines indicate different percentage corrections  $W_{\text{HI}}$ . Horizontal colored dashed lines indicate the uncertainties  $\sigma_{W_{\text{HI}}} = \sigma_{N_{\text{HI}}}/C$  for the three components in the NEP field, from Table 3.

tion  $W_{\text{HI}}$  pixel by pixel in NEP, distinguishing each of the three velocity range components. This log–log plot reveals an approximate quadratic dependence of the correction in  $W_{\text{HI}}$  (such a line is plotted), so that the fractional corrections scales as  $W_{\text{HI}}$ , potentially rising above the uncertainty  $\sigma_{N_{\text{HI}}}/C$ . The spread in this figure is consistent with expectations from simple model spectra using Gaussian components. The vertical height at a given  $W_{\text{HI}}$  is inversely related to the line width and the vertical spread is also influenced by the amount of overlap of the components in velocity.

This correction can be compared to the typical uncertainty in  $N_{\text{HI}}$  discussed in Appendix D. For NEP a value  $\sigma_{N_{\text{HI}}}$  of  $0.2 \times 10^{19} \text{ cm}^{-2}$  from Table 3 corresponds to  $W_{\text{HI}} \sim 1 \text{ K km s}^{-1}$ . Any opacity correction below this limit can be ignored. Above this limit, LVC is affected at the 2–8% level; the uncertainty in the correction will of course be less than this. Some IVC is affected in this same range but other IVC much less. The HVC component is least affected by any opacity (at the lower left the upturn relative to quadratic relates to the positive definite nature of the correction even for low  $T_b$ ).

In Figure 12 we present maps of this first-order correction for the LVC and IVC components in NEP. The HVC correction, not shown, is minimal and below the

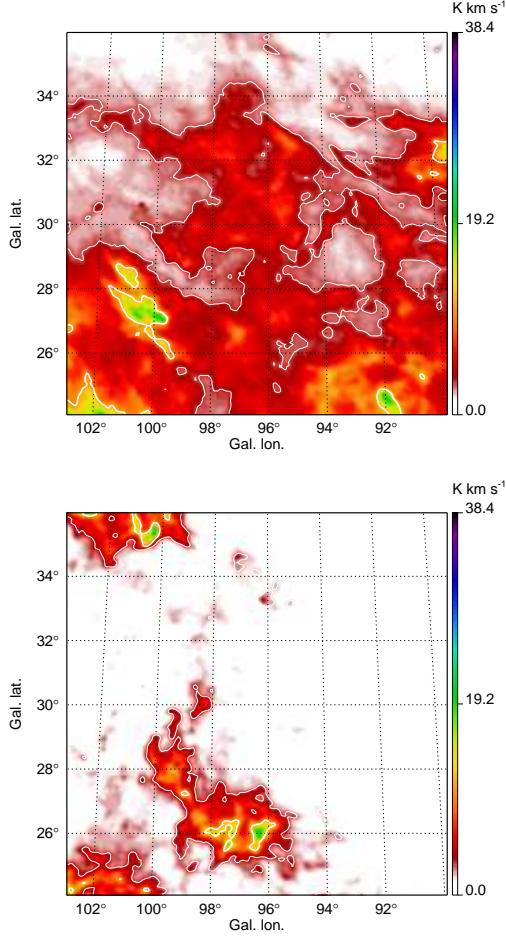


**Figure 12.** Map of the first order correction,  $1/(2T_s) \int T_b^2 dv$ , for NEP (upper: LVC, lower: IVC). Here we set  $T_s = 80$  K. Note that the range in the colorbar is smaller by a factor of ten compared to that for the corresponding  $W_{\text{HI}}$  maps in Figure 5. The two contours show the (full) correction as a percentage of  $W_{\text{HI}}$  (2.5% and 5%). The HVC correction is minimal and so is not shown.

noise (Figure 11). These appear like non-linear representations of  $W_{\text{HI}}$  in Figure 5. Also note the relative scales. A few contours show the (full) correction as a fraction of  $W_{\text{HI}}$ . Thus from Figures 11 and 12 both LVC and IVC components contain regions where opacity in the line is non-negligible and thus an uncertainty arises in the derivation of  $N_{\text{HI}}$ , dependent on the choice of  $T_s$  and more profoundly on the assumption of a constant  $T_s$ .

### C.3. Assessment using all GHIGLS Spectra

Given the approximate quadratic dependence seen in Figure 11, it is advantageous to divide out one power of the dependence of the opacity correction on  $W_{\text{HI}}$ , so that the fractional correction  $(N_{\text{HI}}(T_s)/C - W_{\text{HI}})/W_{\text{HI}}$  is seen to be approximately linear in  $W_{\text{HI}}$ . This is plotted in Figure 13 for a single  $T_s = 80$  K as a two-dimensional histogram using the values for every pixel in our component  $W_{\text{HI}}$  maps of all fields. The various islands, or ridges, within the two-dimensional histogram arise because the line profiles leading to a given  $W_{\text{HI}}$  can be different: broad with low  $T_b$  and so a smaller correction, or narrow and peaked and so more affected.

Also shown in the solid contours is the first-order correction for the same  $T_s$ . The agreement is excellent at

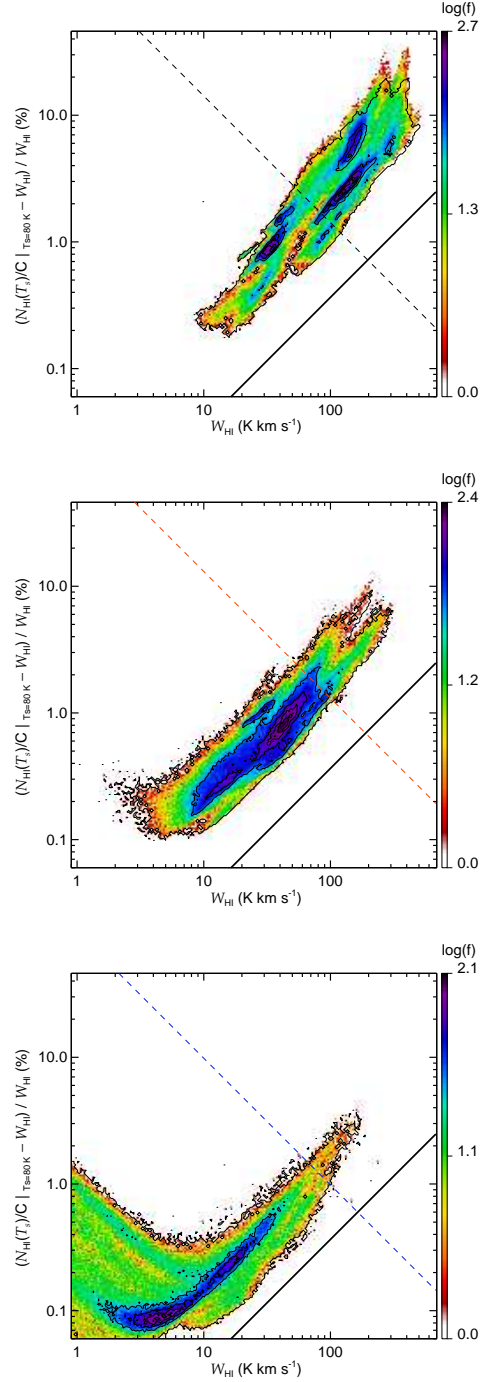


**Figure 13.** Histogram of full fractional correction  $(N_{\text{HI}}(T_s)/C - W_{\text{HI}})/W_{\text{HI}}$  calculated for  $T_s = 80$  K for all pixels in our component  $W_{\text{HI}}$  maps of all GHIGLS fields. Upper: LVC; middle: IVC; lower: HVC. A common line segment of slope one, transferred from Figure 11, reveals the approximate linear dependence. The solid contours, representing the first-order correction for the same  $T_s$ , show that this approximation remains quite good even at the highest values of  $W_{\text{HI}}$  encountered. The dashed lines, also from Figure 11, are for typical values of the uncertainties  $\sigma_{N_{\text{HI}}}/C$  in  $N_{\text{HI}}/C$  for those components (from the NEP values in Table 3). The correction in the HVC component is rarely above this uncertainty. IVC and LVC are progressively more affected, having typically higher  $W_{\text{HI}}$ , and so making an appropriate and accurate correction is more of a concern.

low  $W_{\text{HI}}$  as expected and remains quite good even at the highest values of  $W_{\text{HI}}$  in these intermediate latitude fields. This difference is much less than the uncertainty that arises from which value of  $T_s$  to adopt.

We have repeated this, but for  $T_s = 200$  K. To verify that the scaling is approximately inversely proportional to  $T_s$  for the full correction, we have multiplied the latter correction by 200/80 and overlaid contours on a figure like Figure 13. Again the agreement is excellent at low  $W_{\text{HI}}$  as expected and it remains quite good even at the highest values of  $W_{\text{HI}}$  encountered.

#### C.4. Impact on Applications of $N_{\text{HI}}$ Maps

As mentioned above, maps of  $N_{\text{HI}}$  have a variety of applications. For example, in Planck Collaboration XXIV (2011) the GHIGLS  $N_{\text{HI}}$  maps were used in conjunction with maps of thermal dust emission to examine regional differences in the dust emissivity, the amount of emission per  $N_{\text{HI}}$ . To identify lines of sight along which there is a significant amount of hydrogen in molecular form, for which  $N_{\text{HI}}$  would no longer be representative of the total column density, a masking procedure was developed. This was based empirically on the presence of emission in excess of that expected from the correlation at lower  $N_{\text{HI}}$  in a particular field. In retrospect the masked regions include all lines of sight in which CO is detected using the Type-3 *Planck* CO map (Planck Collaboration XIII 2014), but the masked region is larger than this, which is interpreted as the presence of molecular, but CO-dark, gas for which the H I diagnostic signal is therefore “missing.” Qualitatively, there might be some ambiguity because  $N_{\text{HI}}$  could be underestimated if not corrected for opacity and indeed the masked regions include areas with bright  $T_b$  and significant opacity such as in Figure 12. However, the  $N_{\text{HI}}$  maps used were already corrected for opacity using  $T_s = 80$  K. In principle, one could account for the excess dust emission by lowering  $T_s$  below 80 K on a pixel-by-pixel basis, producing a map of  $T_s$  in the masked region. In this solution, many lines of sight would require  $T_s$  to conspire to be as low as the peak  $T_b$  in the spectrum. Assuming that this is not allowed and that  $T_s = 80$  K is a reasonable value for the entire field as justified earlier in this section, the excess dust emission cannot be accounted for by an insufficient opacity correction. Furthermore, the purpose of the masking was to exclude regions in which  $N_{\text{HI}}$  might not be a good tracer of total column density, and  $N_{\text{HI}}$  in the retained regions is certainly not sensitive to the choice of  $T_s$ . Thus by excluding regions with the masking procedure, the analysis of dust emissivity in the atomic gas is not significantly impacted by uncertainty in the opacity correction.

However, often the full  $N_{\text{HI}}$  map is desirable, as in the power spectrum analysis. The appropriateness and impact of using the corrected  $N_{\text{HI}}$  in such a situation can be guided by a sensitivity analysis to gauge the robustness of the derived results when different values of  $T_s$  are adopted. For example, in the power spectra of  $N_{\text{HI}}$  corresponding to the analysis of  $N_{\text{HI}}$  component maps in NEP in Section 7.1 and Figure 6 with  $T_s = 80$  K, if no correction is applied then the power spectra are only minimally steeper ( $< 0.02$ ).

#### D. ASSESSMENT OF UNCERTAINTY IN $N_{\text{HI}}$

As discussed by Boothroyd et al. (2011), there are a number of distinct contributions that affect the accuracy of the spectra: noise, baseline fitting errors, and errors in the subtraction of the stray radiation spectrum. Because the column density is such an important data product for subsequent analyses, we focus here on the related question of the uncertainty  $\sigma_{N_{\text{HI}}}$  in  $N_{\text{HI}}$  (for this discussion,  $N_{\text{HI}}$  is used interchangeably with  $W_{\text{HI}}$ , other than the scaling parameter  $C$  as in Equation (1)). The results have been given in Table 3.

The following subsections summarize our understanding of the behavior of the various contributions. This exercise also involves various checks on the quality of the GHIGLS data, including a critical look for systematic errors.

##### D.1. Noise in Emission-free Channels

In emission-free channels, the noise  $\sigma_{\text{ef}}$  can be measured as the rms fluctuations about zero in a spectrum or, alternatively, in a single channel map in the cube. The same noise can be assessed from the width of the peak near zero in a histogram of  $T_b(x, y, v)$ . For our basic observation and processing – a single mapping of a field with 4 s integration per spectrum and modified Bessel interpolation into a cube with  $0.8 \text{ km s}^{-1}$  channels – the measured noise,  $\sigma_0$ , is typically 110 mK. With a total of  $n_m$  repeats of the mapping, this is found to go down as  $\sigma_0/\sqrt{n_m}$  as expected. Measured values of the typical  $\sigma_{\text{ef}}$  for various GHIGLS fields are summarized in Table 1.

Because we are working with column density  $N_{\text{HI}}$  here, we are interested in how the noise increases when  $n_c$  channel maps are summed. For  $n_c$  independent emission-free channels, for a single mapping with  $\sigma_0 \sim 110 \text{ mK}$  the expected rms error in  $N_{\text{HI}}$  would be  $0.14 \times 10^{19} \sqrt{n_c/75} \text{ cm}^{-2}$  and for the GHIGLS observations this can be scaled by  $\sigma_{\text{ef}}/\sigma_0 (< 1)$ . This error is consistent with what is found directly from the rms of maps of the sum of emission-free channels (see also Section D.2.1). The choice of 75 channels for the illustrative normalization is a reasonable one, being close to the median number of channels in the component intervals in Table 2; it represents a velocity interval of  $60 \text{ km s}^{-1}$ .

##### D.2. Power Spectrum of the Noise

As is apparent from the dots in Figure 6, the shape of the power spectrum of the noise is not flat (i.e., white) at  $k > 0.1 \text{ arcmin}^{-1}$ , but instead has a characteristic decrease at the largest  $k$  that arises from correlations induced by the modified Bessel function interpolation of each observed H I spectrum onto the grid (Section 3.2). We have verified the precise form of this decrease through simulations, starting with a white noise channel map that is subsequently spatially filtered (convolved) to correspond to the modified Bessel function interpolation used in the gridding of our data.

When we sum a number of emission-free channels in our observed cube and compute its power spectrum, at high  $k$  the shape of this power spectrum is the same regardless of the number of channels. Furthermore, this same shape is seen in the  $N_{\text{HI}}$  data itself (Figure 6). Therefore the noise can be quantified simply by a “noise

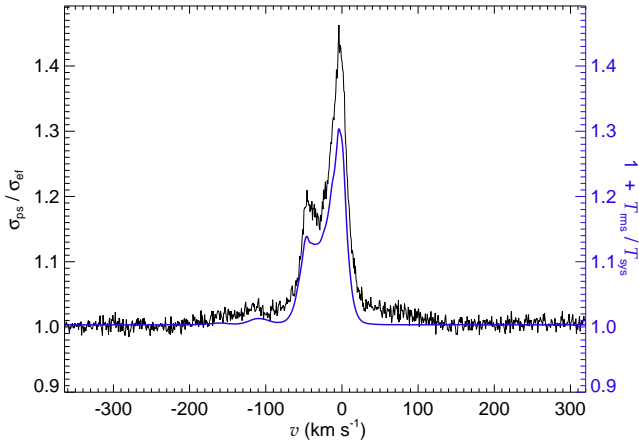


**Figure 14.** Estimate of the noise in each channel of the NEP cube from the power-spectrum analysis,  $\sqrt{\eta} = \sigma_{\text{ps}}/\sigma_{\text{ef}}$  (Appendix D.2.1). At the ends of the spectrum  $\sqrt{\eta} \sim 1$ , as expected for primarily emission-free channels. However, where there is signal the estimated noise is somewhat larger. To model the contribution of noise arising from the 21-cm emission itself, we use the approximation  $1 + \text{rms } T_{\text{b}}(v)/20 \text{ K}$ , based on the rms  $T_{\text{b}}$  measured in each channel map (Appendix D.3). The resulting smooth curve (right axis) captures some basic features of the increase in noise.

template,”  $N(k)$ , and a scale factor,  $\eta$ . This is reflected in the full parameterized model of the one-dimensional power spectrum in Equation (5). We use the fitted level  $\eta$  as a quantitative diagnostic of the noise (from all sources) in the map. We denote as  $\sigma_{\text{ps}}$  the estimate of the rms noise in a map that is derived using this power-spectrum analysis. From this complementary approach estimates of  $\sigma_{N_{\text{HI}}}$  for the component  $N_{\text{HI}}$  maps of the GHIGLS fields have been entered in Table 3.

#### D.2.1. Noise Template

In this paper the noise template used is that derived from emission-free end channels. This can be quantified by  $\sigma_{\text{ef}}$ , the rms noise of the inverse Fourier transform of this noise template. Because the same template, simply scaled by  $\eta$ , is used in the power-spectrum analysis we have  $\sigma_{\text{ps}} = \sqrt{\eta}\sigma_{\text{ef}}$ .

As an example, power-spectra of the NEP cube can be modelled on a channel by channel basis using Equation (5) to find  $\eta$ . The resulting spectrum  $\sqrt{\eta} = \sigma_{\text{ps}}/\sigma_{\text{ef}}$  is shown in Figure 14. This  $\sqrt{\eta}$  spectrum approaches unity in the velocity ranges  $-350 < v < -250 \text{ km s}^{-1}$  and  $175 < v < 275 \text{ km s}^{-1}$  because these are the ranges of the typical end channels used to remove baselines. The end channels used vary from spectrum to spectrum across the field. In these velocity ranges over 99% of the pixels in each channel have been used to determine a baseline. This also demonstrates that the noise template is defined consistently.

As another application, we made  $N_{\text{HI}}$  maps from an increasing number of channels of a simulated noise cube and found the expected behavior  $\eta \propto n_{\text{c}}$ , or  $\sigma_{\text{ps}} \propto \sqrt{n_{\text{c}}}$ . Fitting baselines has a notable effect on the accumulation of noise. To demonstrate this we fit baselines in this noise cube, using data where the emission-free end channels would normally be, and subtracted them.

For  $N_{\text{HI}}$  maps made from channels where baselines were fit the noise  $\eta$  first increases with  $n_{\text{c}}$  but eventually reaches a maximum and turns over when  $n_{\text{c}}$  is compara-

ble to the range used to fit the baselines, the exact point depending on the degree of the polynomial baseline being fit. This effect is a result of the correlations introduced by the baseline fitting. We examined the NEP cube in the same way and found a similar behavior with increasing  $n_{\text{c}}$ .

For the channels where there is signal, away from where the baselines are defined, the noise is somewhat larger than simply  $\sigma_{\text{ef}}$  (Figure 14). This will affect the noise in  $N_{\text{HI}}$  maps too; the noise estimated from the sum of emission-free channels will always be an underestimate.

#### D.3. Noise in the Line Emission

The 21-cm line emission itself increases the noise by a factor approximately  $1 + T_{\text{b}}(v)/T_{\text{sys}}$  (Boothroyd et al. 2011) and because the GBT 21-cm receiver noise is so low ( $T_{\text{sys}} \sim 20 \text{ K}$ ) the increase can be significant even in the GHIGLS fields.

This additional noise will not be uniform across the channel map, but the size of the effect can be demonstrated using a representative  $T_{\text{b}}(v)$ . For each channel map we adopted the rms value,  $\text{rms } T_{\text{b}}(v)$ , noting that this spectrum is the sum in quadrature of the mean and standard deviation spectra seen in Figure 4. The approximate increase in the noise spectrum predicted on this basis,  $1 + \text{rms } T_{\text{b}}(v)/20 \text{ K}$ , is shown for NEP in Figure 14. It captures basic features of the increase seen in the actual noise spectrum.

#### D.4. Baseline Errors

Fitting and subtracting a baseline introduces errors in  $N_{\text{HI}}$  through uncertainties in the fitted coefficients. Baseline errors add to the increased noise apparent in the shoulders adjacent to the emission-free channels in Figure 14 and to the channels with more significant emission as well.

This will propagate to uncertainty in  $N_{\text{HI}}$  maps too. Unlike the noise in the line emission, baseline errors are similar for adjacent channels in a spectrum and so accumulate as  $n_{\text{c}}$ . Boothroyd et al. (2011) showed that these amount to an uncertainty in  $N_{\text{HI}}$  typically  $0.3 \times 10^{19} (n_{\text{c}}/75) \text{ cm}^{-2}$ , comparable to the noise estimates above for  $n_{\text{c}} \sim 75$  but with a different  $n_{\text{c}}$  dependence. This was found by comparing independent XX and YY polarization cubes. These cubes have common stray radiation and so their difference (XX–YY) reflects the quality of baselines plus thermal noise (which can be seen increasing where there is a signal).

The assumption made in both Planck Collaboration XXIV (2011) and Boothroyd et al. (2011) is that the noise in the difference and the noise in the sum are identical. This is not the entire story, as we demonstrated by examination of the power spectra for a single observation of a subfield of NEP. We produced maps of  $W_{\text{HI}}$  from both XX+YY and XX–YY cubes. The power-spectrum analysis yielded slightly larger values of  $\sigma_{\text{ps}}$  in the XX+YY case, by up to 25%.

#### D.5. Errors in the Stray Radiation Spectrum

Boothroyd et al. (2011) showed that there is a significant error contribution to  $N_{\text{HI}}$  from the uncertainty in the predicted stray radiation spectrum that is subtracted. This is an error that can vary slowly over a field

in the course of mapping and like the baseline removal could have a non-linear effect on the scaling parameter of the noise power spectrum.

An empirical approach to determining this uncertainty is to compare the reproducibility of  $N_{\text{HI}}$  derived from cubes made from different independent mappings of a field (up to three in our survey). This includes all sources of error but is dominated by the accumulated baseline errors and the imperfect stray radiation subtraction. In principle it would be possible to schedule observations to make repeated maps with virtually the same stray radiation. However, in practice because of our exploitation of flexible scheduling the mapping of (parts of) any field took place at different times of day, on different days, and at different times of year, and so generally the stray radiation and the estimated correction are different in different maps of the same field. Indeed, this was used by Boothroyd et al. (2011) to study the properties of the stray radiation and to calibrate the amplitude of the sidelobes in the all-sky response of the GBT. A corollary is that because the stray radiation can now be predicted in advance, future observations could be scheduled for times at which the stray radiation is minimized. The data reported in this paper for the faint N1 field approach this ideal.

For every GHIGLS field in addition to the observed emission-line cube we have a predicted stray radiation cube from which we can compute  $N_{\text{HIstray}}$ . Using the above difference approach, Boothroyd et al. (2011) showed that the error contribution to  $N_{\text{HI}}$  is of order  $0.07 N_{\text{HIstray}}$ .

Because the errors in two repeated observations  $i$  and  $j$  are independent, and ultimately the two are averaged together to form  $\langle N_{\text{H}} \rangle = (N_{\text{H},i} + N_{\text{H},j})/2$ , the estimator of interest in assessing errors in  $N_{\text{HI}}$  is the dispersion (the standard deviation about the mean) of the map of  $\Delta N_{\text{H}} = (N_{\text{H},i} - N_{\text{H},j})/2$ , or for the complementary approach being used here  $\sigma_{\text{ps}}$  from the power-spectrum analysis of that difference map.

Again using the power-spectrum analysis to find  $\sigma_{\text{ps}}$  we are able to look at not only the noise in the repeat observation difference maps, but also the noise in their sum. The disagreement between the results is somewhat greater than in the analysis of XX and YY used to study baseline errors. The power-spectrum analysis yielded  $\sigma_{\text{ps}}$  values for the sum roughly 50% larger than for the difference.

## E. COMPARISON WITH DATA FROM EBHIS

A thorough comparison of our GHIGLS data with that from the LAB survey was performed in Boothroyd et al. (2011). Here we compare our data with that from the Effelsberg-Bonn H I Survey (EBHIS) (Flöer et al. 2010; Winkel et al. 2010; Kerp et al. 2011; Winkel et al. 2012) with the goal of testing the quality of the GHIGLS data and the data reduction procedures, especially the correction for stray radiation. The EBHIS collaboration has provided unpublished data cubes and stray radiation cubes for the NEP field that has been used for many illustrations in this paper, another large field centred on SPIDER but including portions of POL, SP, SPC, and UMA (these all relate to the NCP loop and so we use the designation NCPLEB here), and DRACO.

### E.1. EBHIS Data and GHIGLS Modifications

The EBHIS data have an angular resolution (FWHM)  $\sim 10'.5$  (Winkel et al. 2010) on a Galactic SFL grid with  $3'2564$  pixels (we regridded to the GHIGLS  $3'.5$ ) and a channel spacing of  $\Delta v = 1.288 \text{ km s}^{-1}$ . The noise maps for all three cubes are presented in the first column of Figure 15 where the EBHIS maps have been cropped to match the coverage of the equivalent GHIGLS field. The noise in each map pixel is set by the rms of emission-free channels in the corresponding spectrum. The mean noise is  $\sigma_{\text{ef}} \sim 95 \text{ mK}$  (NEP),  $\sim 86 \text{ mK}$  (NCPLEB), and  $\sim 90 \text{ mK}$  (DRACO).

For a direct comparison with EBHIS, the GHIGLS data cubes first need to be convolved to the slightly lower resolution of the EBHIS survey. Following the convolution of each channel in the cubes, the GHIGLS data were regridded both spatially (cubic convolution interpolation using the IDL routine *interpolate*) and along the velocity axis (linear interpolation). These steps of convolution and regridding reduce the original noise of the GHIGLS data for NEP, NCPLEB, and DRACO from 68 mK, 75/105 mK,<sup>14</sup> and 61 mK (Table 1) by about a factor 2 to an average rms noise 34 mK, 40/55 mK, and 31 mK, respectively. The rms noise maps for the modified GHIGLS data are shown in the right column of Figure 15.

The scanning and map-making strategies are reflected in the various geometric (grid) patterns (called GPs below) that appear in these noise maps. In addition, spectra with very few emission-free end channels due to the presence of galaxies result in noise peaks in these maps.

### E.2. Relative Calibration

Prior to detailed comparisons between EBHIS and GHIGLS, we first determine if correction by a scale factor is necessary. This is done by comparing  $T_{\text{b}}$  along every common line of sight, fitting the scatter plots using the anticipated linear model:

$$\text{EBHIS} = a \times \text{GHIGLS} + b. \quad (\text{E1})$$

This is repeated for scatterplots of  $W_{\text{HI}}$  as well. Both correlations are very good.

The scale factor (slope)  $a$  should be close to unity, but reflects the different methods by which the spectra have been calibrated. In the ideal case, there would be no offset  $b$ . However, inconsistencies remaining after the stray radiation and/or baseline corrections can introduce an offset and this can in turn influence the slope. These inconsistencies and noise will have the largest relative effect where  $T_{\text{b}}$  is small. To ensure that the derived scale factor is not influenced unduly we limit the data to  $T_{\text{b}} > T_{\text{limit}}$ . The regression is repeated on each field for many values of  $T_{\text{limit}}$  while also varying the velocity range over which the data are fit. Not surprisingly the velocity components in which the spectra have the largest range in  $T_{\text{b}}$  yield the most robust fits.

We find that  $a$  and  $b$  vary slightly as a function of  $T_{\text{limit}}$  and velocity component and that in general the derived slopes and offsets are anti-correlated. With the assumption that errors from removal of stray radiation and baseline will result in both over- and under-corrections

<sup>14</sup> Values for SPIDER but the flanking fields are similar.

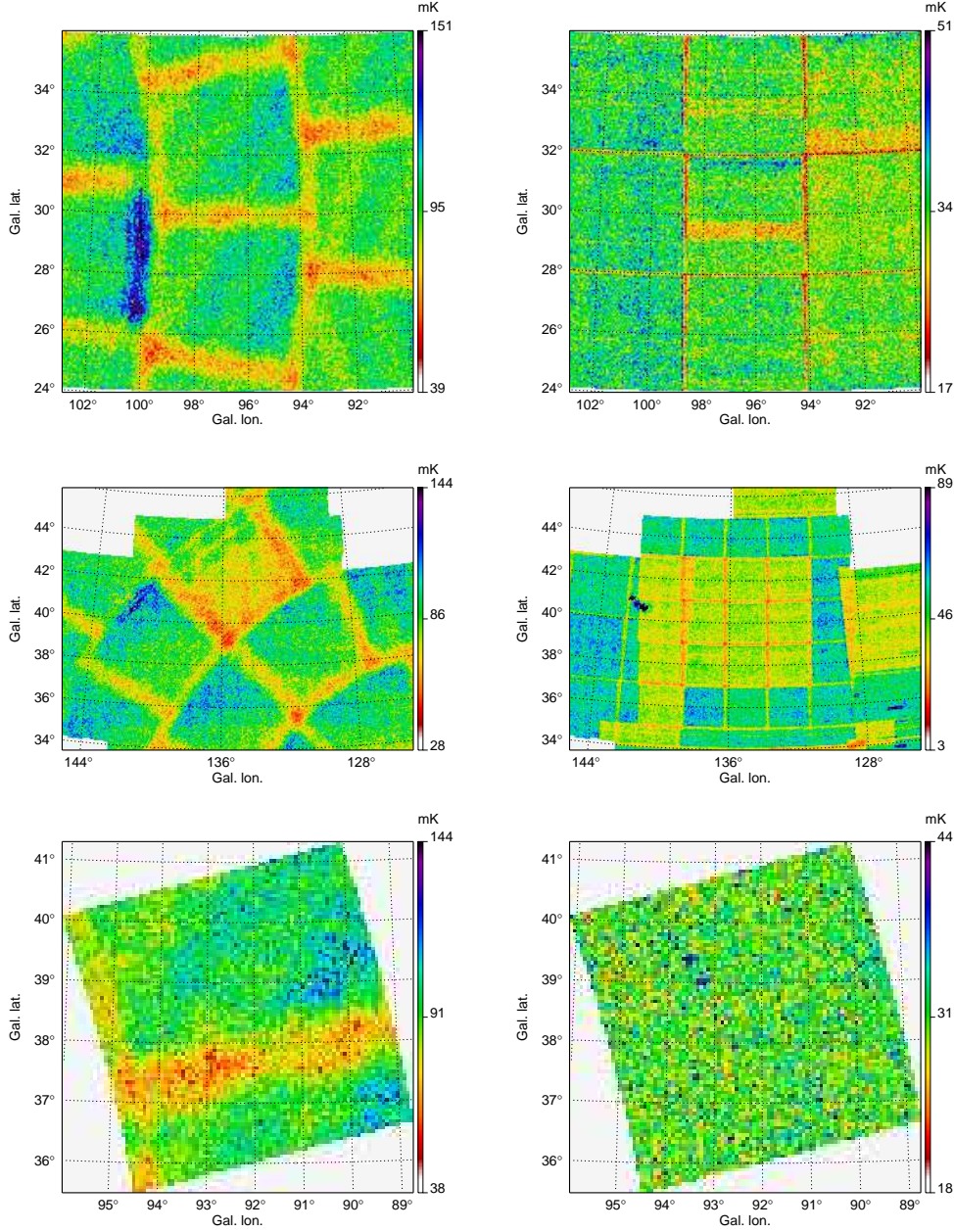


**Figure 15.** Left: Noise map for EBHIS produced from the rms in emission-free channels in each spectrum. Right: Noise map for the GHIGLS data adjusted to the same resolution and same gridding. Top to bottom respectively: NEP, NCPLEB, and DRACO. EBHIS maps have been cropped to match the available GHIGLS coverage. Large scale patterns in the noise reflect the different observing strategies. Note that the angular scale and the central value and range of the colorbar are different for each map. In NCPLEB emission in the M81 – M82 system is sometimes challenging for both GHIGLS and EBHIS, causing some artifacts within about a degree of  $(l, b) = (142^\circ, 41^\circ)$ .

in both datasets, the most robust slopes would be those with the lowest absolute offsets. For each velocity component we look for the  $T_{\text{limit}}$  that satisfies this criterion and also check for the relative constancy of the slope over a neighboring range in  $T_{\text{limit}}$ . The scale factors derived from the  $T_b$  and  $W_{\text{HI}}$  analyses are consistent with one another when there is a suitably large range in  $T_b$  (or  $W_{\text{HI}}$ ; e.g., Table 3) and likewise the results from the three velocity components in each of the three fields examined are also consistent. The dispersion of the different estimates is 0.030. We adopt a scale factor EBHIS/GHIGLS =  $1.009 \pm 0.011$ . Before comparing the spectral data in the analyses below, we made the minor

adjustment of all EBHIS survey data to the GHIGLS scale using this scale factor.

The EBHIS and GHIGLS calibrations are consistent to within 1%. From Boothroyd et al. (2011) the GHIGLS calibration has a formal uncertainty of 1% and there we concluded conservatively that “our calibration does not have systematic errors that exceed a few percent.” We recall that our previous comparison with the LAB survey over all GHIGLS fields resulted in a scale factor LAB/GHIGLS =  $1.0288 \pm 0.0012$  (Boothroyd et al. 2011).

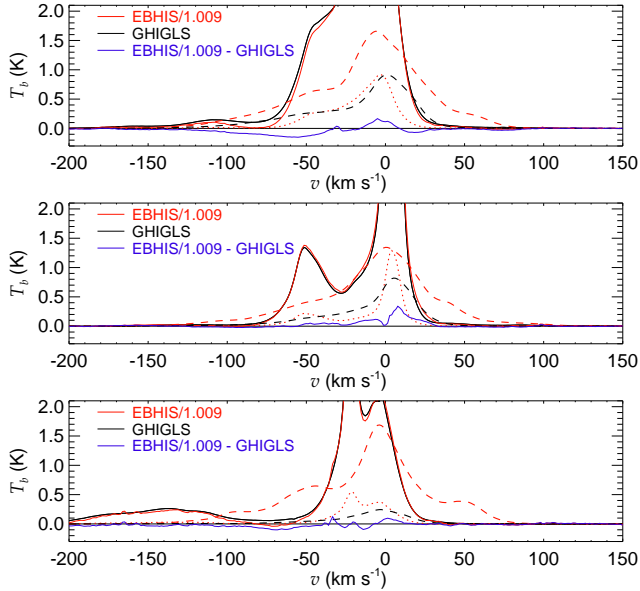


**Figure 16.** Top panel: Average GHIGLS spectrum for NEP (black), average scaled EBHIS spectrum (red), residual scaled EBHIS – GHIGLS (blue). Average GHIGLS spectrum peaks at 5.7 K. Broken lines show the average spectra of the predicted stray radiation that has been removed from the data; dashed for GHIGLS (black) and dashed and dotted (red) for EBHIS far and near side lobes, respectively. Following panels: Average spectrum for NCPLEB peaking at 8.1 K and for DRACO peaking (in the IVC) at 3.8 K.

### E.3. Mean and Individual Spectra

As shown by the average spectra for EBHIS and (convolved and regridded) GHIGLS in each field in Figure 16, and the difference spectrum, there is remarkable agreement between the two surveys. Also shown are the average spectra of the predicted stray radiation that have been subtracted in producing these spectra. For EBHIS, the stray radiation spectrum is calculated in two parts, for the near and far side lobes (Kalberla et al. 2010). The GBT has an unblocked aperture, but there is a significant spillover sidelobe from the secondary reflector (Boothroyd et al. 2011). Obviously, the stray radiation is substantial in fields such as surveyed by GHIGLS so that without its removal the spectra would be quite different and there would be no agreement between the surveys. The spectral extent of the stray radiation is larger for the far sidelobes where Doppler effects are more significant, well into HVC velocities in the case of EBHIS.

Individual spectra, though noisier, show similar features. Figure 17 compares an EBHIS spectrum with the corresponding (convolved and regridded) GHIGLS spectrum for three distinct lines of sight. The NEP spectrum has strong relative emission in the LVC range. The NCPLEB spectrum was selected for its relatively large GHIGLS predicted stray radiation spectrum. The DRACO spectrum has strong relative emission in the IVC range. The difference spectra confirm that the overall agreement is very good.

### E.4. Comparisons of Maps of $W_{\text{HI}}$

In this section we look for evidence in the GHIGLS spectra for errors that might be attributable to uncertainties in the baselines that were fit and subtracted or to imperfect predictions of the stray radiation spectrum

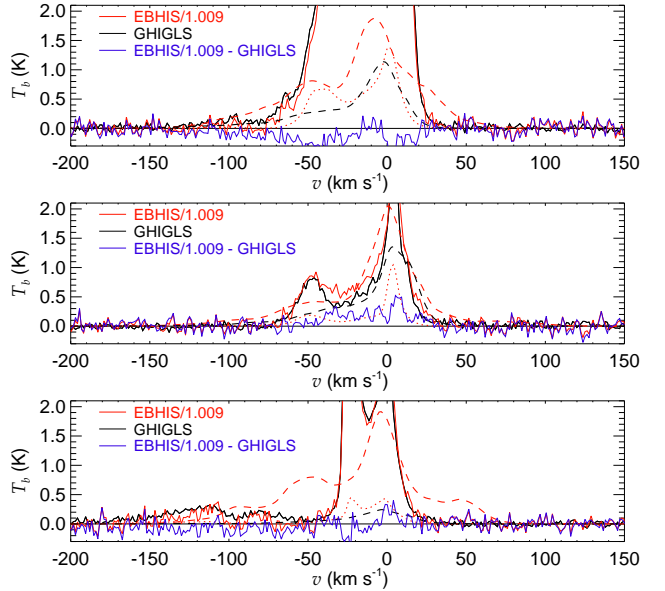


**Figure 17.** Same as Figure 16 but for individual spectra. Top panel: NEP spectrum at  $(99^{\circ}7, 27^{\circ}0)$  peaking at 18.7 K. Following panels: NCPLEB spectrum at  $(137^{\circ}6, 38^{\circ}1)$  peaking at 3.2 K and DRACO spectrum at  $(90^{\circ}0, 38^{\circ}7)$  peaking (in the IVC) at 17.7 K. that has been subtracted. The EBHIS survey provides an independent basis for this assessment.

Each of these two contributions is somewhat correlated from one channel to the next and thus any errors are more easily seen in the line integral  $W_{\text{HI}}$ . Additionally, the velocity dependence of these components suggests that any  $W_{\text{HI}}$  comparison should be made over restricted ranges of velocity (e.g., using LVC, IVC, and HVC components as defined in Table 2). Consequently we produce a series of  $W_{\text{HI}}$  maps corresponding to these velocity components.

In the analysis below of these maps we find some evidence for errors relating to the subtraction of baselines and stray radiation. These errors are at a low level, consistent with the slight increase of  $\sigma_{N_{\text{HI}}}$  over the value expected from noise in the line emission alone (Appendix D). Overall the GHIGLS and EBHIS maps are in good agreement.

#### E.4.1. Data

Figure 18 shows the data available for this investigation. The field is NEP. The columns (left to right) are for integrals over the LVC, IVC, and HVC velocity intervals. Unless otherwise indicated, in all of the panels the range for the colorbar extends from the minimum to maximum of the data values and is usually quite different from one panel to another.

The first row contains the  $W_{\text{HI}}$  contributions from the baselines that have been fit and subtracted in producing the GHIGLS cubes. The second row shows the contributions from the predicted stray radiation for GHIGLS that has also been subtracted. In the third row are the  $W_{\text{HI}}$  maps from GHIGLS already seen in Figure 5. The range of the colorbar starts at zero and extends to the 99% percentile. For the residual maps in the fourth row we have first computed the  $W_{\text{HI}}$  maps from the EBHIS spectra, adjusted as above to the GHIGLS scale, and then subtracted the GHIGLS  $W_{\text{HI}}$  maps. Here the colorbar is centered on the mean and has a total range that is



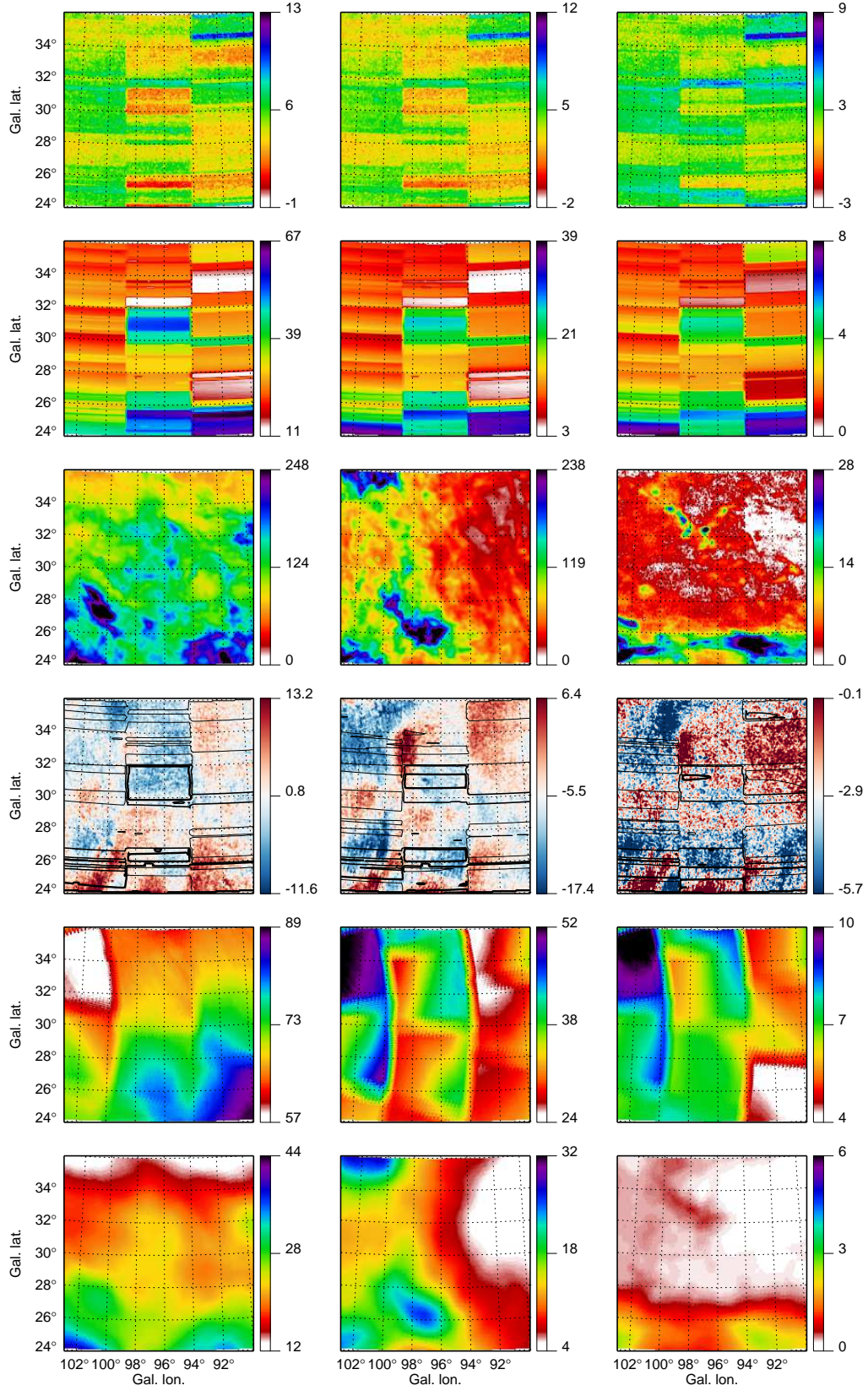


**Figure 18.**  $W_{\text{HI}}$ -related maps of the NEP field (see text in Section E.4.1 for details). Columns (left to right) are for integrals over the LVC, IVC, and HVC velocity intervals. Rows (top to bottom) are from the following data: GHIGLS baselines (subtracted in producing GHIGLS  $W_{\text{HI}}$ ), GHIGLS stray radiation (subtracted), GHIGLS  $W_{\text{HI}}$  (as in Figure 5),  $W_{\text{HI}}$  residual from scaled EBHIS – GHIGLS, EBHIS far sidelobe (subtracted in producing EBHIS  $W_{\text{HI}}$ ), and EBHIS near sidelobe stray radiation (subtracted). On the residual map are overlaid contours from the GHIGLS stray radiation map (from thinnest to thickest at 25%, 50%, and 75% of the maximum value) for reference and orientation.

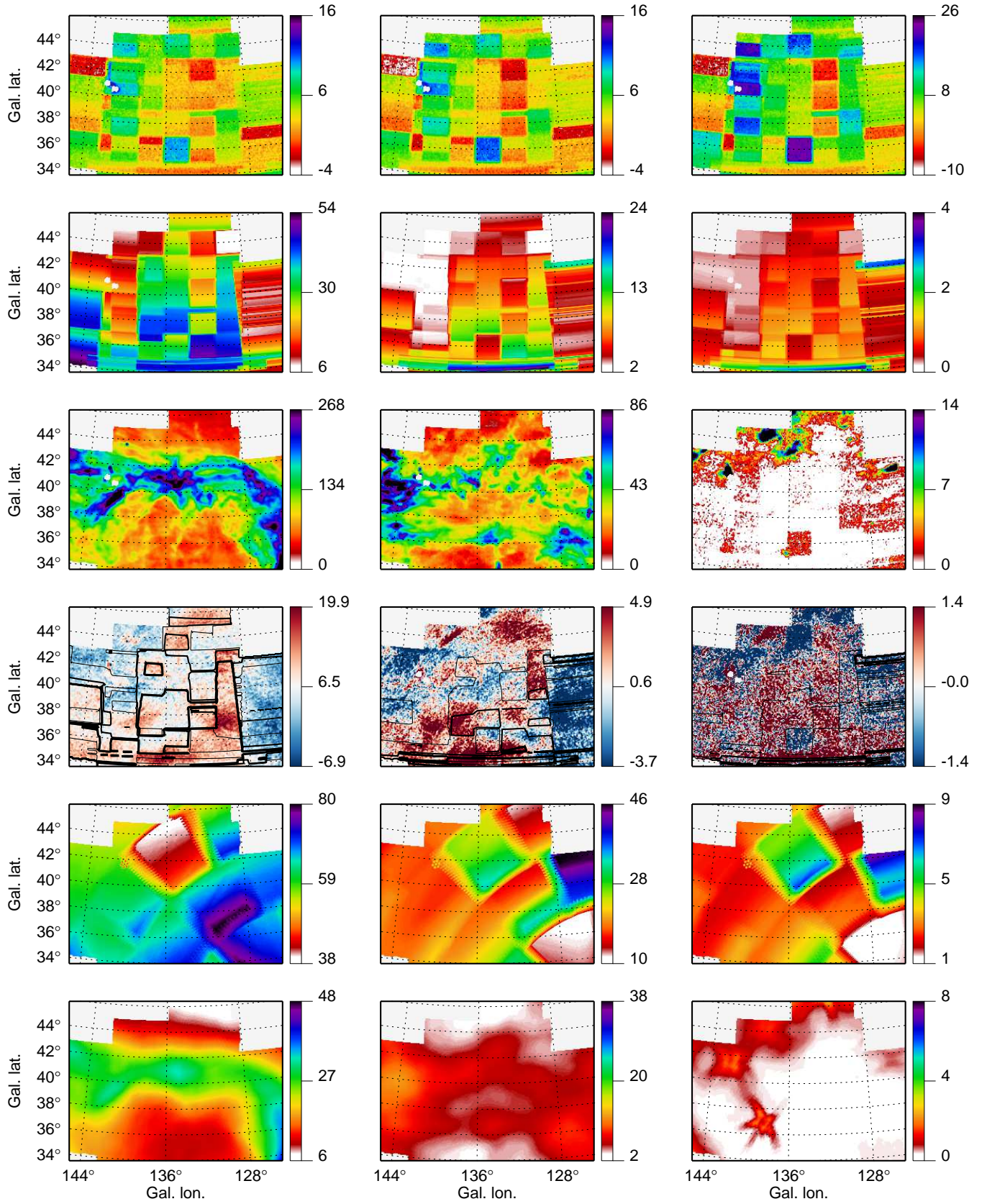


**Figure 19.** Same as Figure 18 for NCPLEB. In the GHIGLS-related maps, pixels are excluded where it was not possible to fit a simple baseline because of emission from other galaxies present in the (frequency-switched) spectrum. Pixels near M81 and M82 where it is not possible to fit a baseline are masked and not used in subsequent analysis. A useful indicator of scale is the pattern of the EBHIS multibeam system that appears imprinted at one position in the maps of the far sidelobe emission in row five.

10% (20% for HVC) of that in the  $W_{\text{HI}}$  map above it. A different color table has been used to emphasize the positive and negative excursions. The fifth and sixth rows show the contributions from the predicted stray radiation for the far and near sidelobes that have been subtracted in producing the EBHIS cubes. The near sidelobe stray radiation map is like a blurred version of the original  $W_{\text{HI}}$  map in row three and is therefore roughly correlated with the signal. Note that the dynamic range spanned by the colorbar is set to be the same as for the far sidelobe map, revealing that the corrections for the near sidelobe emission are generally much smaller.

Figure 19 contains the corresponding  $W_{\text{HI}}$ -related maps for NCPLEB.

Even more so than in Figure 15 there are different GPs that are obvious in rows one and two and in rows five and six. The GPs are related to the scanning strategies of the respective surveys and how the observation blocks were organized and scheduled. Given their origins the GPs are not correlated with the astronomical  $W_{\text{HI}}$  signal in row three, except as already noted for the EBHIS near sidelobe stray radiation in row six.

A strategy for identifying sources of systematic effects/errors is to search for corresponding telltale patterns like the GPs in the residual maps, i.e., is there a “smoking gun” revealing anything amiss with any of these corrections?

#### E.4.2. Residual Map

As can be seen from the relative dynamic ranges of the maps, the baseline and stray radiation corrections that have been subtracted from the GHIGLS and EBHIS data are significant. To the extent that they have been accurately calculated – and because the data from the two telescopes have been set to a common calibration scale – the residual maps should appear structureless and centred on zero, reflecting solely the combined  $W_{\text{HI}}$  noise. This is not quite the case.

The residual map is centered on zero for the LVC component in NEP and the IVC and HVC components in NCPLEB, and there are broad areas in other maps where this is the case too. But when the average residual spectrum in Figure 16 is systematically non-zero over a considerable velocity range, for example the negative residual in the IVC and HVC components in NEP, then this will also be the case for the mean of the  $W_{\text{HI}}$  residual map.

On the residual map we show contours from the GHIGLS stray radiation maps to highlight the patchwork of largely rectangular patterns relating to the observing blocks (the GPs) for reference and orientation. In size and orientation the GPs for EBHIS are quite different from those for GHIGLS (see also Figure 15).

The residual map is defined as scaled EBHIS – GHIGLS. GHIGLS has been produced from the original data minus the corrections in the top two rows and so if a correction there were too large it would produce an excess in the residual map. Similarly EBHIS has been produced from the original data minus the corrections in the bottom two rows and so if a correction there were too large it would produce a deficit in the residual map.

#### E.4.3. Noise in the Line Emission

The noise in the line emission of the two surveys, of order  $\sigma_{\text{ef}} \times [1.0 + T_{\text{b}}(v)/(20 \text{ K})]$  (see Appendix D.3), accumulates as  $\sqrt{n_c} \Delta v$  to contribute fluctuations  $\delta W \sim 0.9 \text{ K km s}^{-1}$  in the residual maps for NEP (0.6 to  $1.3 \text{ K km s}^{-1}$  depending on the field and velocity component, the larger values in the more extensive HVC intervals).<sup>15</sup> These fluctuations are small compared to the range shown in the residual maps, but do contribute to the graininess everywhere. Note that the noise in the line emission would not produce any systematic offset in the maps.

#### E.4.4. Errors Related to Fitted Baselines

The GHIGLS baselines tend to be fairly stable within a given scheduled observing block, and this is reflected in the rectangular GPs in the first row of maps. The measured standard deviation within a rectangle, typically  $0.5 \text{ K km s}^{-1}$  in NEP ( $0.3$  to  $1.1 \text{ K km s}^{-1}$  overall), contributes to the graininess in the residual maps. The measured standard deviation in large smooth areas of the residual maps is typically  $1.5 \text{ K km s}^{-1}$  in NEP ( $1.5$  to  $1.9 \text{ K km s}^{-1}$  overall). Our interpretation is that this can be accounted for by the noise in the line emission and the baseline fluctuations, including those of EBHIS which we have not attempted to quantify. However, we note that there are low-amplitude striped patterns in the EBHIS and residual maps that can be discerned along the distinctively oriented scan lines of EBHIS, with a spacing related to the multibeam system, for example in the IVC component in NEP and the LVC and IVC components in NCPLEB. The measured peak-to-peak amplitude of the pattern is small, of order  $2 \text{ K km s}^{-1}$ .

The GHIGLS baselines do vary from observing block to observing block. Just as the GHIGLS baselines are fairly stable within the rectangular GPs, any errors in the mean offsets within these rectangles are likely to be correlated, which could produce a corresponding pattern in the residual map. As discussed below, the magnitude of such rectangle to rectangle systematic errors is of the same order as the above-mentioned fluctuations and therefore not normally readily discerned in the residual maps given the range of values therein. However, the stray radiation correction and the range in the residual maps generally decrease steadily from LVC to HVC, making HVC  $W_{\text{HI}}$  maps the most favourable for investigating the baseline errors.

A special case to examine is the large  $60 \text{ deg}^2$  region in NCPLEB ranging in  $l$  from  $125^\circ$  and  $145^\circ$  and in  $b$  from  $34^\circ$  to  $40^\circ$  in which there is virtually no HVC emission detectable (see the column of HVC maps in Figure 19). In the GHIGLS  $W_{\text{HI}}$  map there are clear GPs relating to the observation blocks used, whereas the EBHIS  $W_{\text{HI}}$  map (not shown) is featureless, and so this rectangular pattern appears (in reverse) in the residual map. Within rectangles in the GHIGLS  $W_{\text{HI}}$  map the standard deviation is  $0.5 \text{ K km s}^{-1}$  whereas the standard deviation for the region as a whole is  $1.0 \text{ K km s}^{-1}$ , from which we deduce that the typical dispersion in the mean amplitudes of rectangles is  $0.9 \text{ K km s}^{-1}$ . We also note that even with

<sup>15</sup> In the GHIGLS  $W_{\text{HI}}$  maps themselves the fluctuations would be  $\sim 0.3 \text{ K km s}^{-1}$  for NEP ( $0.2$  to  $0.7 \text{ K km s}^{-1}$  overall).

these clearly visible GPs in the GHIGLS  $W_{\text{HI}}$  map, the standard deviation is still slightly smaller than it is in the smooth EBHIS  $W_{\text{HI}}$  map ( $1.1 \text{ K km s}^{-1}$ ). The GHIGLS stray radiation correction map has the same GPs, but its overall low level ( $0.7 \pm 0.3 \text{ K km s}^{-1}$ ) and the fact that it is uncorrelated with the observed pattern in  $W_{\text{HI}}$  make it an unlikely source. On the other hand there is a weak positive correlation of the pattern in  $W_{\text{HI}}$  with that in the baseline correction map. Thus we conclude that small observing block to observing block errors in the baseline correction with dispersion of about  $1 \text{ K km s}^{-1}$  are the likely source of the pattern; this would correspond to a rectangle to rectangle dispersion in mean offsets in  $T_{\text{b}}$  of  $8 \text{ mK}$  over this entire HVC velocity interval. The origin of this is unknown but could be related to the general problem of interpolating a low-order function over a large range. Even when the function is well-constrained by the data in many emission-free end channels, the large range over which the function is interpolated introduces an error. For completeness, we note that the average  $W_{\text{HI}}$  in this HVC region is  $0.04 \text{ K km s}^{-1}$  for GHIGLS and  $0.34 \text{ K km s}^{-1}$  for EBHIS. This small difference of  $0.3 \text{ K km s}^{-1}$ , the mean of the residual map in this region, is in accord with the difference in the average spectrum (like Figure 16); this difference could be due to small errors in baselines and/or in the stray radiation corrections.

Where there is faint but significant HVC emission detected by GHIGLS in large regions of NEP above  $27^\circ$ , and also in DRACO, we find a negative residual, i.e., EBHIS underestimates this emission by a few  $\text{K km s}^{-1}$ . We interpret this as a result of the different sensitivities of the two surveys combined with modelling of the baselines. The GHIGLS residual baseline is fit iteratively with a third-degree polynomial (Boothroyd et al. 2011), whereas the EBHIS baseline is determined using an iterative Gaussian smoothing technique (Winkel et al. 2010) applied over their entire bandwidth of  $100 \text{ MHz}$ . Note that the EBHIS data were observed with a frequency-switching of  $3 \text{ MHz}$ , but due to the gain varying as a function of frequency, the data were not reduced using the frequency-switching technique (Winkel et al. 2010); thus the need for a more sophisticated algorithm to remove the baseline. Empirically, the sign of the offset indicates that the lower sensitivity (higher noise) of the EBHIS spectra may result in a fitted baseline that eliminates part of what in GHIGLS is detected as HVC emission rather than elevated baseline. Likewise, the GHIGLS data baseline fitting could be removing signal that with more sensitive observations would lead to the detection of resolved structure.

As mentioned, baseline fitting procedures are not as successful at determining and removing a baseline when the emission from galaxies dramatically reduces the number of emission-free channels and/or significantly dominates the shaping of the baseline.

#### E.4.5. Stray Radiation

In Figure 16 at HVC velocities the average residual spectrum contains only low frequency oscillations, consistent with a low-order polynomial used to model baselines. This can be contrasted with the sharper oscillations in the LVC and IVC ranges, which must derive from errors other than the baseline. This sharper struc-

ture, also discernible in the residuals of individual spectra in Figure 17, will affect the LVC and IVC  $W_{\text{HI}}$  residual maps. The residuals for these components are larger than for the HVC. Furthermore, because of the larger dynamic range of the stray radiation corrections in the LVC and IVC velocity intervals, these intervals are the most favorable for looking for any errors arising because of uncertainties in the stray radiation corrections.

For GHIGLS there is no direct spatial correlation between the stray radiation and  $W_{\text{HI}}$  because of the unblocked geometry of the GBT design. Instead, for intermediate latitude fields such as these the amount of stray radiation is strongly influenced by the time at which any given observation is made because of how the offset spillover sidelobe beam pattern (Boothroyd et al. 2011) overlaps (or not) with the stronger emission near the Galactic plane. This results in a rectangular pattern in the stray radiation map relating to the observational blocks used. The stray radiation corrections for EBHIS are also significant and the maps have quite different morphological structure.

There are some smoking guns. In the NEP residual map for IVC in Figure 18 there are triangular shapes that are clearly anti-correlated in amplitude with the EBHIS far sidelobe stray radiation correction. To a lesser extent there is a positive correlation discernible for LVC. In the NCPLEB residual map for LVC in Figure 19 there are rectangular shapes with a clear positive correlation in amplitude with the GHIGLS stray radiation correction. This persists somewhat in the IVC.

Attempting some quantification and motivated by this suggestion of multiplicative factors, we sought to reduce the standard deviation of the residual maps by removing correlations with various combinations of the stray radiation maps. For example, in the case of IVC in NEP, a factor  $-0.4$  of the EBHIS far sidelobe correction is indicated (in the case of LVC the factor is  $+0.2$ ). However, while this lowers the standard deviation of the residual map from  $4.6$  to  $3.7 \text{ K km s}^{-1}$  it is clearly not the whole story. There is still a rectangular pattern in the revised residual map that reveals the GHIGLS observational scheduling blocks, but it is not multiplicatively related at a significant level ( $> -0.1$ ). Telltale signs of the GPs of both GHIGLS and EBHIS stray radiation corrections in the revised residual maps indicate clearly that there are substantial additive and/or subtractive errors too, which make any multiplicative factor uncertain. Accounting for these errors is even more important than the multiplicative changes to reduce the standard deviation in the residual to a level about  $1 \text{ K km s}^{-1}$  that could be expected from baseline fitting errors and line noise alone. If we suppose that the entire  $4.6 \text{ K km s}^{-1}$  dispersion is roughly equally apportioned to GHIGLS and EBHIS (thus  $3.2 \text{ K km s}^{-1}$  each), then this amounts to about a  $10\%$  fraction of the mean stray radiation corrections (an even small fraction in the case of LVC). However, we feel that it is probably better to think of the errors in absolute terms rather than as a fractional error.

For our NCPLEB LVC example, a factor  $+0.2$  of the GHIGLS stray radiation correction is indicated (the stray radiation correction has been overestimated). In this case this appears to be much larger than the estimated  $W_{\text{HI}}$  stray radiation uncertainty of a factor  $0.07$  found by Boothroyd et al. (2011). But again the standard

deviation of the residual map is only lowered from 4.5 to 3.6 K km s<sup>-1</sup> and there are still telltale signs of the schedule-related GPs of both GHIGLS and EBHIS stray radiation corrections in the original and revised residual maps.

We have carried out a similar comparative study in DRACO. In the GHIGLS observations of this field, which is a relatively faint extension off the upper right of the much larger NEP field, the stray radiation corrections are fortuitously at the low end of the values encountered in the NEP observations. However, this makes it more difficult to spot any errors in these corrections. On the other hand the EBHIS far sidelobe stray radiation correction is quite large and its pattern is discernible particularly on the IVC residual map. But because the standard deviation of the residual map is already so low (2.6 K km s<sup>-1</sup>) it is difficult to draw any definitive conclusions, except of course that the corrections applied in both surveys are very good. This can be appreciated as well in the agreement of the mean spectra in Figure 16.

#### F. COMPARISON WITH DATA FROM GASS

Here we compare our data with that from the southern hemisphere-based H I Galactic All-Sky Survey (GASS) (McClure-Griffiths et al. 2009; Kalberla et al. 2010; Kalberla & Haud 2015) available in the GASS III data release repository.<sup>16</sup> Because of the latitude coverage of the GASS data and our choice of primarily northern circumpolar fields for the surveys with the GBT ACS, we have only one field available for this comparison, MC. In extracting the GASS cube we adopted an optimal modified Bessel function mapping of the data onto a 4'8 grid using the gridding parameters recommended by Mangum et al. (2007). This is similar but not identical to our modified Bessel function mapping of the GHIGLS spectra onto a GLS grid (see Section 3.2). The downloaded GASS cube has angular resolution  $\sim 16'$  (modified from the original average 14'4 due to our gridding choice) on a Cartesian Equatorial grid, 0.82 km s<sup>-1</sup> channels, and an empirically-determined noise of  $\sigma_{\text{ef}} \sim 47$  mK.

The GHIGLS data cube was convolved to this lower resolution and regridded in all dimensions. This reduces the noise from the original 83 mK (Table 1) to an effective noise 17 mK.

Following the same analysis as in Appendix E.2, these GASS data appear to be brighter than GHIGLS by a factor GASS/GHIGLS = 1.062 ± 0.019. This is in agreement with the conclusion arrived at independently by Kalberla & Haud (2015) who compared GASS to EBHIS and LAB (LDS).

On adjusting the GASS data to the GHIGLS scale we again find remarkable agreement as demonstrated in the spectra in Figure 20. Also shown there are the stray radiation corrections that have been applied to the GHIGLS and the GASS data.

As in Appendix E.4 we produced a series of  $W_{\text{HI}}$  maps for each velocity component (Table 2) and present them in Figure 21. The residual maps confirm the overall good agreement of the two data sets.

In the HVC part of the spectrum (the largest range, adopting -153.4 km s<sup>-1</sup> to -32.9 km s<sup>-1</sup> from Table 2)

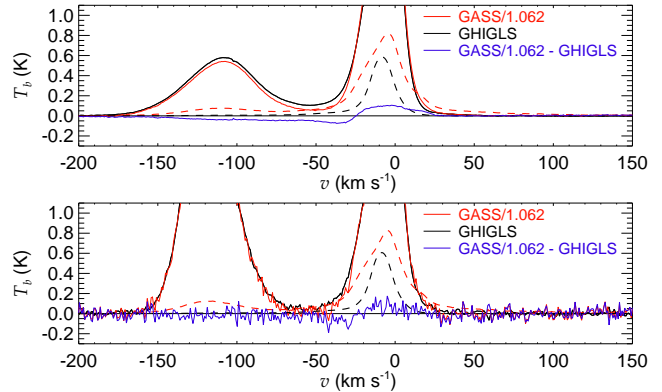


**Figure 20.** Top panel: Average GHIGLS spectrum for MC (black), average scaled GASS spectrum (red), residual GASS - GHIGLS (blue). Dashed line spectra are the average stray radiation predictions that have been removed from the data. The MC average spectrum peaks at 3.2 K. Bottom panel: Individual MC spectrum at (59°4, -81°5) with relatively strong HVC emission peaking at 2.5 K (LVC peaks at 3.0 K). Note the different  $T_b$  range as compared to Figures 16 and 17.

the residual in the average spectrum (Figure 20) is negative and therefore so is the residual map for that component, which has a mean  $-4.8$  K km s<sup>-1</sup>. The GHIGLS stray radiation correction is small by comparison and there is no clear imprint of the morphology of the GASS stray radiation correction in the  $W_{\text{HI}}$  residual map. This suggests that the origin of the offset might be in the modelling of the baselines. The GASS instrumental baseline was removed by an iterative procedure (Kalberla et al. 2010; Kalberla & Haud 2015) using either a 9th- or 11th-order polynomial over a much larger bandwidth than used for GHIGLS for which a third-degree polynomial could be used (Boothroyd et al. 2011). With the lower sensitivity of the GASS measurements the fitting of the baseline between the main emission peaks in the profile might include what in GHIGLS is detected as emission, thus raising the baseline and lowering the apparent signal, consistent with the sign of the offset.

Over the IVC range (the smallest,  $-32.9$  km s<sup>-1</sup> to  $-8.8$  km s<sup>-1</sup>) the residual in the average spectrum changes sign producing a net effect consistent with the near-zero mean ( $+0.7$  K km s<sup>-1</sup>) in the  $W_{\text{HI}}$  residual map. The dynamic range in both stray radiation corrections is small and in the residual map there is no telltale sign of errors in these corrections. However, the location and abruptness of the sign change in the residual spectra is suggestive of small errors in the stray radiation corrections, rather than in the baselines.

Over the LVC range ( $-8.8$  km s<sup>-1</sup> to  $+48.3$  km s<sup>-1</sup>) the positive residual in the average spectrum results in a slightly positive mean ( $+2.3$  K km s<sup>-1</sup>) in the  $W_{\text{HI}}$  residual map. There are again no unequivocal signs of errors in the stray radiation corrections that have been applied.

In the GASS data, including the noise map and the stray radiation corrections and propagating to the  $W_{\text{HI}}$  residual maps, there is a slight hatching pattern related to the orientation of the GASS scans and the multibeam system, but this has no bearing on the other considerations here.

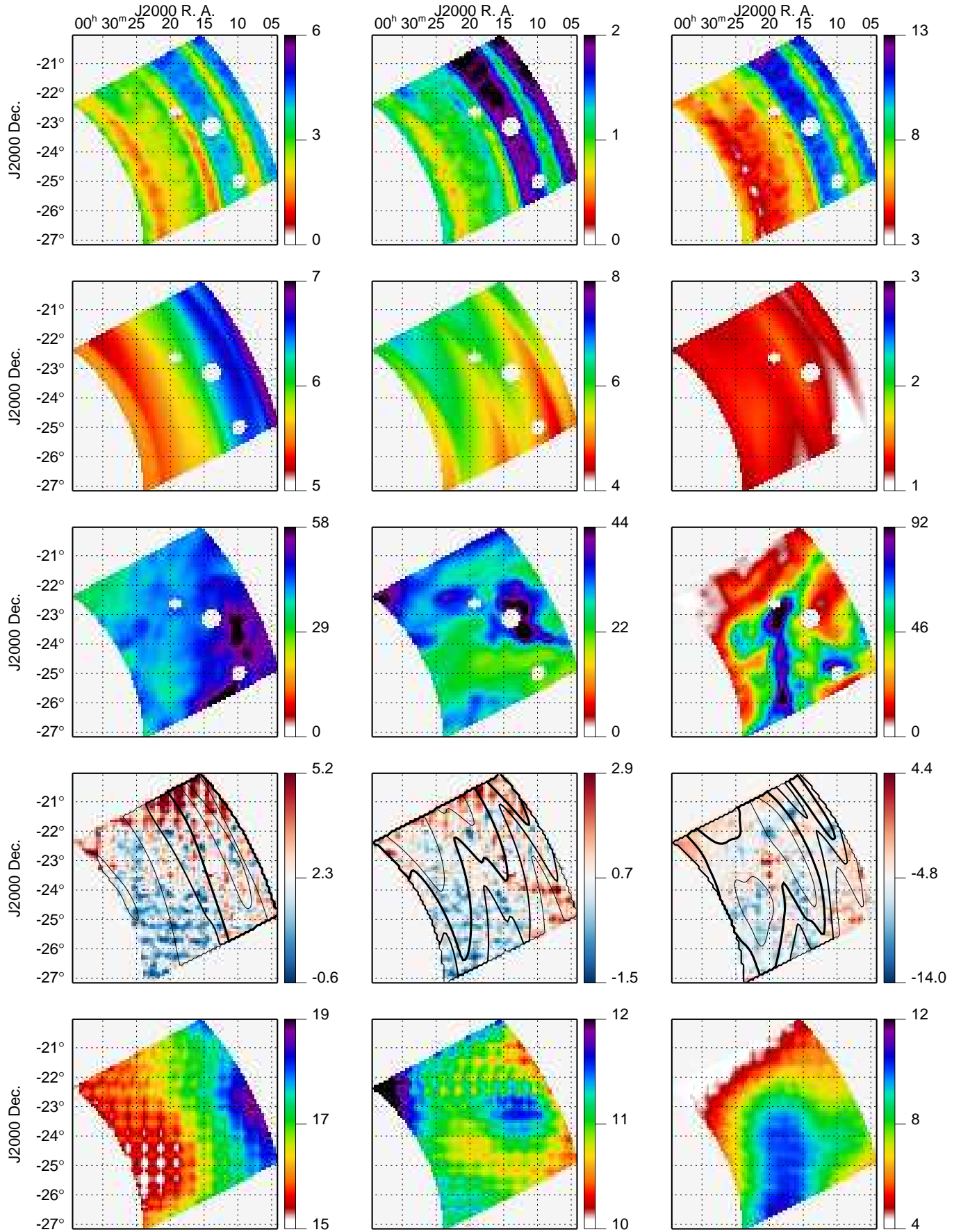


**Figure 21.** Same as Figure 18 for MC and comparison with GASS rather than EBHIS. There is only one stray radiation correction cube for GASS. Note the areas masked because of the effects of the galaxies MCG-04-02-003, NGC 0045, and NGC 0024 (from left to right).

- Arendt, R. G., Odegard, N., Weiland, J. L., et al. 1998, *ApJ*, 508, 74 **1.2**
- BICEP2/Keck Array and Planck Collaborations. 2015, *Phys. Rev. Lett.*, 114, 101301 **1.2**
- Blagrove, K., Lockman, F. J., & Martin, P. G. 2010, in *Astronomical Society of the Pacific Conference Series*, Vol. 438, *Astronomical Society of the Pacific Conference Series*, ed. R. Kothes, T. L. Landecker, & A. G. Willis, 156 **1**
- Boothroyd, A. L., Blagrove, K., Lockman, F. J., et al. 2011, *A&A*, 536, A81 **1, 3, 3.1, 6.1, 3, 8.1, 10, A, D, D.3, D.4, D.5, E, E.2, E.3, E.4.4, E.4.5, F**
- Boulanger, F., Abergel, A., Bernard, J., et al. 1996, *A&A*, 312, 256 **1.2**
- Boulanger, F., & Perault, M. 1988, *ApJ*, 330, 964 **1.2**
- Bregman, J. N. 1980, *ApJ*, 236, 577 **1.1**
- Burton, W. B. 1976, *ARA&A*, 14, 275 **1**
- Cabral, B., & Leedom, L. C. 1993, in *Special Interest Group on GRAPHics and Interactive Techniques Proceedings.*, *Special Interest Group on GRAPHics and Interactive Techniques Proceedings.*, 263–270 **10**
- Calabretta, M. R., & Greisen, E. W. 2002, *A&A*, 395, 1077 **3.2**
- Clark, S. E., Peek, J. E. G., & Putman, M. E. 2014, *ApJ*, 789, 82 **1.2**
- Crovisier, J., & Dickey, J. M. 1983, *A&A*, 122, 282 **1.1**
- Davis, M., Guhathakurta, P., Konidaris, N. P., et al. 2007, *ApJ*, 660, L1 **2.1.1**
- Deshpande, A. A., Dwarakanath, K. S., & Goss, W. M. 2000, *ApJ*, 543, 227 **7.1**
- Deul, E. R., & Burton, W. B. 1992, in *Saas-Fee Advanced Course 21: The Galactic Interstellar Medium*, ed. W. B. Burton, B. G. Elmegreen, & R. Genzel, 79–99 **1.2**
- Dickey, J. M., & Lockman, F. J. 1990, *ARA&A*, 28, 215 **1, 1.1**
- Dickey, J. M., McClure-Griffiths, N. M., Gaensler, B. M., & Green, A. J. 2003, *ApJ*, 585, 801 **1.1, C**
- Dickey, J. M., McClure-Griffiths, N. M., Stanimirović, S., Gaensler, B. M., & Green, A. J. 2001, *ApJ*, 561, 264 **1.1**
- Dickey, J. M., Strasser, S., Gaensler, B. M., et al. 2009, *ApJ*, 693, 1250 **8.2, C, C.1**
- Dole, H., Le Floc’h, E., Pérez-González, P. G., et al. 2004, *ApJS*, 154, 87 **2.1.3**
- Flöer, L., Winkel, B., & Kerp, J. 2010, in *RFI Mitigation Workshop*, 42 **E**
- Gautier, III, T. N., Boulanger, F., Perault, M., & Puget, J. L. 1992, *AJ*, 103, 1313 **1.1, 7.1**
- Giacconi, R., Rosati, P., Tozzi, P., et al. 2001, *ApJ*, 551, 624 **2.1.1**
- Gillmon, K., Shull, J. M., Tumlinson, J., & Danforth, C. 2006, *ApJ*, 636, 891 **2.1.6, C**
- Grogin, N. A., Kocevski, D. D., Faber, S. M., et al. 2011, *ApJS*, 197, 35 **2.1.1**
- Grossan, B., Heiles, C., & Peek, J. E. G. 2012, in *American Astronomical Society Meeting Abstracts*, Vol. 219, *American Astronomical Society Meeting Abstracts #219*, #349.23 **B**
- Hasinger, G., Altieri, B., Arnaud, M., et al. 2001, *A&A*, 365, L45 **2.1.1**
- Haud, U. 2000, *A&A*, 364, 83 **1.1, 8**
- Haud, U., & Kalberla, P. M. W. 2007, *A&A*, 466, 555 **1.1, 8.1, C.1**
- Heiles, C. 1976, *ApJ*, 208, L137 **1**
- Heiles, C., & Troland, T. H. 2003, *ApJ*, 586, 1067 **1.1, 8.2, C, C.1**
- Hennebelle, P., & Falgarone, E. 2012, *A&A Rev.*, 20, 55 **1.1, 7, 7.1, 8.3, C.1**
- Herbstmeier, U., Heithausen, A., & Mebold, U. 1993, *A&A*, 272, 514 **2.1.3**
- Hornscheimer, A. E., Brandt, W. N., Garmire, G. P., et al. 2001, *ApJ*, 554, 742 **2.1.1**
- Jahoda, K., Lockman, F. J., & McCammon, D. 1990, *ApJ*, 354, 184 **2.1.1**
- Jannuzi, B. T., & Dey, A. 1999, in *Astronomical Society of the Pacific Conference Series*, Vol. 191, *Photometric Redshifts and the Detection of High Redshift Galaxies*, ed. R. Weymann, L. Storrie-Lombardi, M. Sawicki, & R. Brunner, 111 **2.1.3**
- Jones, M. H., Rowan-Robinson, M., Branduardi-Raymont, G., et al. 1995, *MNRAS*, 277, 1587 **1.2**
- Kalberla, P. M. W., Burton, W. B., Hartmann, D., et al. 2005, *A&A*, 440, 775 **1, 1**
- Kalberla, P. M. W., & Haud, U. 2015, *A&A*, accepted, arXiv:1505.01011 **8.1, F, F**
- Kalberla, P. M. W., & Kerp, J. 2009, *ARA&A*, 47, 27 **1**
- Kalberla, P. M. W., McClure-Griffiths, N. M., Pisano, D. J., et al. 2010, *A&A*, 521, A17 **E.3, F, F**
- Kerp, J., Winkel, B., Ben Bekhti, N., Flöer, L., & Kalberla, P. M. W. 2011, *Astronomische Nachrichten*, 332, 637 **E**
- Kim, J., & Ryu, D. 2005, *ApJ*, 630, L45 **13**
- Krumpe, M., Miyaji, T., Brunner, H., et al. 2015, *MNRAS*, 446, 911 **2.1.4**
- Kulkarni, S. R., Heiles, C., & Blitz, L. 1982, *ApJ*, 259, L63 **1**
- Lazarian, A., & Pogosyan, D. 2000, *ApJ*, 537, 720 **1.1**
- Lockman, F. J., & Condon, J. J. 2005, *AJ*, 129, 1968 **1.2, A**
- Lockman, F. J., Jahoda, K., & McCammon, D. 1986, *ApJ*, 302, 432 **2.1.1, 2.1.4**
- Lockman, F. J., Martin, P. G., Miville-Deschênes, M.-A., & Boulanger, F. 2005, in *Bulletin of the American Astronomical Society*, Vol. 37, *American Astronomical Society Meeting Abstracts*, 1301 **2.1.3**
- Lonsdale, C. J., Smith, H. E., Rowan-Robinson, M., et al. 2003, *PASP*, 115, 897 **2.1.1**
- MacDonald, E. C., Allen, P., Dalton, G., et al. 2004, *MNRAS*, 352, 1255 **2.1.1**
- Magnani, L., Blitz, L., & Mundy, L. 1985, *ApJ*, 295, 402 **2.1.6**
- Mangum, J. G., Emerson, D. T., & Greisen, E. W. 2007, *A&A*, 474, 679 **3.2, F**
- Markwardt, C. B. 2009, in *Astronomical Society of the Pacific Conference Series*, Vol. 411, *Astronomical Data Analysis Software and Systems XVIII*, ed. D. A. Bohlender, D. Durand, & P. Dowler, 251 **7.1**
- Martin, P. G., Rogers, C., Reach, W. T., Dewdney, P. E., & Heiles, C. E. 1994, in *Astronomical Society of the Pacific Conference Series*, Vol. 58, *The First Symposium on the Infrared Cirrus and Diffuse Interstellar Clouds*, ed. R. M. Cutri & W. B. Latter, 188 **1.2, 2.1.3**
- McClure-Griffiths, N. M., Pisano, D. J., Calabretta, M. R., et al. 2009, *ApJS*, 181, 398 **F**
- Meyerdierts, H., Heithausen, A., & Reif, K. 1991, *A&A*, 245, 247 **2.1.5**
- Miville-Deschênes, M.-A., Boulanger, F., Reach, W. T., & Noriega-Crespo, A. 2005, *ApJ*, 631, L57 **1.2**
- Miville-Deschênes, M.-A., Joncas, G., Falgarone, E., & Boulanger, F. 2003a, *A&A*, 411, 109 **7.1**
- Miville-Deschênes, M.-A., Lagache, G., Boulanger, F., & Puget, J.-L. 2007, *A&A*, 469, 595 **7, 7.1**
- Miville-Deschênes, M.-A., Lagache, G., & Puget, J.-L. 2002, *A&A*, 393, 749 **7**
- Miville-Deschênes, M.-A., Levrier, F., & Falgarone, E. 2003b, *ApJ*, 593, 831 **8.3**
- Miville-Deschênes, M.-A., Martin, P. G., Abergel, A., et al. 2010, *A&A*, 518, L104 **7.1**
- Ouchi, M., Shimasaku, K., Okamura, S., et al. 2001, *ApJ*, 558, L83 **2.1.1**
- Pénin, A., Lagache, G., Noriega-Crespo, A., et al. 2012, *A&A*, 543, A123 **1.2, 2.1.2**
- Pinheiro Gonçalves, D. 2013, PhD thesis, University of Toronto **1.2**
- Pinheiro Gonçalves, D., Martin, P. G., Blagrove, K., & Miville-Deschênes, M. A. 2013, in *Proceedings of The Life Cycle of Dust in the Universe: Observations, Theory, and Laboratory Experiments (LCDU2013)*. 18–22 November, 2013. Taipei, Taiwan. Editors: Anja Andersen (University of Copenhagen, Denmark), Maarten Baes (Universiteit Gent, Belgium), Haley Gomez (Cardiff University, UK), Ciska Kemper (Academia Sinica, Taiwan), Darach Watson (University of Copenhagen, Denmark). Online at [http://pos.sissa.it/archive/conferences/207/113/LCDU2013\\_113.pdf](http://pos.sissa.it/archive/conferences/207/113/LCDU2013_113.pdf) **1.2**
- Planck Collaboration XVIII. 2011, *A&A*, 536, A18 **1.2, 2.1.2**
- Planck Collaboration XIX. 2011, *A&A*, 536, A19 **1.2**
- Planck Collaboration XXIV. 2011, *A&A*, 536, A24 **1.1, 1.2, 2.1.2, 2.1.6, 5, 5, 6.1, C.4, D.4**
- Planck Collaboration I. 2014, *A&A*, 571, A1 **2.1.4**
- Planck Collaboration XI. 2014, *A&A*, 571, A11 **5**
- Planck Collaboration XIII. 2014, *A&A*, 571, A13 **C.4**
- Planck Collaboration XVI. 2014, *A&A*, 571, A16 **7.1**
- Planck Collaboration XXX. 2014, *A&A*, 571, A30 **1.2, 2.1.2**
- Planck Collaboration XXV. 2015, *A&A*, submitted, arXiv:1506.06660 **9**

- Planck Collaboration Int. XVII. 2014, *A&A*, 566, A55 [1.1](#)
- Planck Collaboration Int. XIX. 2015, *A&A*, 576, A104 [9](#), [10](#)
- Planck Collaboration Int. XXX. 2014, *A&A*, in press, arXiv:1409.5738 [1.2](#), [7.1](#)
- Planck Collaboration Int. XXXII. 2014, *A&A*, in press, arXiv:1409.6728 [1.2](#), [9](#)
- Planck Collaboration Int. XXXV. 2015, *A&A*, in press, arXiv:1502.04123 [1.2](#), [9](#)
- Planck Collaboration Int. XXXVIII. 2015, *A&A*, submitted, arXiv:1505.02779 [9](#)
- Prestage, R. M., Constantikes, K. T., Hunter, T. R., et al. 2009, *IEEE Proceedings*, 97, 1382 [1](#)
- Putman, M. E., Peek, J. E. G., & Jounge, M. R. 2012, *ARA&A*, 50, 491 [1](#)
- Reach, W. T., Koo, B.-C., & Heiles, C. 1994, *ApJ*, 429, 672 [1.2](#)
- Reach, W. T., Wall, W. F., & Odegard, N. 1998, *ApJ*, 507, 507 [1.2](#)
- Roy, N., Kanekar, N., & Chengalur, J. N. 2013, *MNRAS*, 436, 2366 [1.1](#)
- Saury, E., Miville-Deschênes, M.-A., Hennebelle, P., Audit, E., & Schmidt, W. 2014, *A&A*, 567, A16 [1.1](#), [5](#), [8](#), [8.1](#), [8.2](#), [8.3](#), [13](#), [C.1](#)
- Sembach, K. R., Wakker, B. P., Tripp, T. M., et al. 2004, *ApJS*, 150, 387 [1.1](#)
- Shapiro, P. R., & Field, G. B. 1976, *ApJ*, 205, 762 [1.1](#)
- Stil, J. M., Taylor, A. R., Dickey, J. M., et al. 2006, *AJ*, 132, 1158 [1](#)
- Strasser, S., & Taylor, A. R. 2004, *ApJ*, 603, 560 [C](#)
- Tripp, T. M., Wakker, B. P., Jenkins, E. B., et al. 2003, *AJ*, 125, 3122 [1.1](#)
- Verschuur, G. L. 2004, *AJ*, 127, 394 [1.1](#)
- Wakker, B. P. 2006, *ApJS*, 163, 282 [2.1.6](#), [C](#)
- Wakker, B. P., Lockman, F. J., & Brown, J. M. 2011, *ApJ*, 728, 159 [6.1](#)
- Wakker, B. P., & Woerden, H. v. 2013, *High-Velocity Clouds*, 587 [1.1](#)
- Winkel, B., Kalberla, P. M. W., Kerp, J., & Flöer, L. 2010, *ApJS*, 188, 488 [E](#), [E.1](#), [E.4.4](#)
- Winkel, B., Kraus, A., & Bach, U. 2012, *A&A*, 540, A140 [E](#)
- Wolfire, M. G., McKee, C. F., Hollenbach, D., & Tielens, A. G. G. M. 2003, *ApJ*, 587, 278 [1.1](#)